This manuscript has been submitted for publication in Geophysical Journal International but has not yet undergone peer review and has yet to be formally accepted for publication. Subsequent versions of this manuscript may have slightly different content. If accepted, the final version of this manuscript will be available via the 'Peer-reviewed Publication DOI' link. The authors welcome feedback on the manuscript.

# Imaging the seismic velocity structure of the crust and upper mantle in the northern East African Rift using Rayleigh wave tomography

Emma L. Chambers[1,2*], Nicholas Harmon[1], Catherine A. Rychert[1], Ryan J. Gallacher[3,4] and Derek Keir[1,5]

[1)] University of Southampton, Southampton, UK

[2)] Dublin Institute for Advanced Studies, Dublin, Ireland

[3)] International Seismological Centre, Pipers Lane, Thatcham, Berkshire, RG19 4NS, UK

[4)] Department of Earth and Environmental Sciences, Tulane University, New Orleans, USA

[5)] Dipartimento di Scienze della Terra, Università degli Studi di Firenze, Florence, Italy

*Corresponding author: Emma L. Chambers (echambers@cp.dias.ie)

Key Points:

- The Ethiopian Plateau has slow velocities in the crust that likely require melt. At mantle depths, off rift velocities do not require melt.
- Beneath the rift, mantle anomalies are punctuated along the rift and offset from the slowest crustal anomalies.
- This suggests that either melt migrates laterally and/ or is ephemeral in a dynamic lithosphere-asthenosphere system.

**Summary**

Within the northern East African Rift, multiple seismic models have been produced to understand the evolution of magmatism, however variations in method, resolution, and scale make direct comparisons challenging. The lack of instrumentation off rift further limits our understanding of the spatial extent of tectonic and magmatic processes, which is crucial to understanding magmatic continental rifting. In this paper, we jointly invert Rayleigh wave dispersion curves from ambient noise and teleseisms to obtain absolute shear velocity maps at 10–150 km depth. This includes data from a new seismic network located on the Ethiopian Plateau and enhanced resolution at Moho and upper mantle depths from the joint inversion. At crustal depths, velocities are slowest beneath the Main Ethiopian Rift and the off rift Ethiopian Plateau (<3.00-3.75 ±0.04 km/s, 10–40 km depth), which are slow enough to require ongoing magmatic emplacement. At 60–80 km depth off rift, we observe a fast velocity lid (>0.1 km/s faster than surroundings), which corresponds to previous estimates of the lithosphere-asthenosphere-boundary. The fast lid is not observed within the rift in locations underlain by asthenospheric slow velocity anomalies (<4.05 ±0.04 km/s at 60–120 km depth), suggesting melt is infiltrating the lithosphere within the rift. Furthermore, the asthenospheric slow velocity anomalies are segmented (~110x80 km wide), existing in areas that have not undergone significant crustal and plate thinning, suggesting segmented melt supply starts prior to significant plate deformation. Finally, the segmented asthenospheric slow velocity zones are not directly located beneath melt-rich crustal regions particularly for those off rift, suggesting mantle melt either migrates laterally during ascent, and/or that melt is ephemeral.

**Key words:** Seismology - Joint inversion - Seismic tomography - Africa - Surface waves and free oscillations

## 1.0 Introduction

Magma injected into the continental lithospheric crust and mantle, and the subsequent weakening and thinning, has been proposed as a mechanism for continental rifting, especially in regions such as the northern East African Rift (EAR) (Buck, 2006). Models and observations of magmatic continental rifting suggest there is melt production and localised emplacement beneath the rift valley (Buck, 2006). However, the locus, depth and along rift variability of melt production and storage remains poorly understood, as does the possibility that magmatic processes occur over a broader region outside the rift valley. Understanding these processes is essential for a full understanding of magmatic continental rifting. The northern EAR is a magmatic rift system where the initial stages of rifting through to incipient seafloor spreading can be observed subaerially (Ebinger & Casey, 2001; Furman et al., 2006). This provides a unique opportunity to study how rifting develops and modifies plate structure through progressive rift sector development (Barberi et al., 1972). A major barrier to understanding magmatic processes subsurface has been that the majority of passive seismic stations were deployed near the rift valley only, preventing comparison to off rift structures. In addition, despite the numerous seismic images created, absolute seismic velocities for the crust and upper mantle are unconstrained beneath a broad region including multiple sectors of the rift and to significant distances off rift (Chambers et al., 2019; Keranen et al., 2009).

Seismic tomography provides constraints on the elastic properties of the Earth, which are used to understand tectonic and magmatic processes. The rift has been extensively imaged, creating multiple velocity models for smaller disparate sections of the region, which are not necessarily directly comparable due to variations in methodology, resolution, and scale. For example, ambient noise tomography (ANT) has been used to produce 3 models of the northern EAR that are not directly comparable due to variations in the type of velocity (phase, group and shear velocity) and regions covered (Afar, central Main Ethiopian Rift and broader rifted regions) (Chambers et al., 2019; Kim et al., 2012; Korostelev et al., 2015). Comparisons between models are important for determining the relationship between magmatic and tectonic processes including variations in plate structure, melt generation and melt migration processes. These comparisons are not possible without a single absolute velocity model that covers the full region. In addition, the rift flanks have not been tomographically imaged at crustal and upper mantle depths due to a lack of instrumentation.

To solve the challenges in comparing multiple models, we produce a comprehensive model by performing a joint inversion between Rayleigh wave dispersion curves from ambient noise and teleseisms to image the absolute seismic shear velocity structure of the nEAR. Our unified model of absolute shear velocity from 10–150 km depth, allows us to determine variations in plate structure both within and off rift. Data is obtained from seismometers present from 1999-2017 located in Ethiopia, Yemen, Djibouti and Eritrea, allowing coverage of regions unaffected by rifting (e.g. west of the Ethiopian Plateau) to areas at incipient seafloor spreading (e.g. Afar). The joint inversion provides increased resolution at lower crustal and uppermost mantle depths which would not be possible with ambient noise or teleseisms individually (Chambers et al., 2019; Gallacher et al., 2016). Furthermore, the addition of the Ethiopian Plateau network allows us to image the transition from unrifted lithosphere to the rift, and obtain a view of the asthenospheric mantle dynamics of rifting at depth. In particular the larger area with increased resolution and improved crustal resolution allows us to compare the presence/absence of slow velocity anomalies likely related to melt in the asthenosphere to those in the crust in a consistent manner to better constrain the pathways of melt and associated dynamics.

## 2.0 Geological Background and Previous Tomographic Studies

Precambrian basement, formed during the Neoproterozoic Pan-African orogeny, underlies much of Ethiopia and the surrounding area (Mège & Korme, 2004). Volcanism initiated 45 Ma and continues to the present day, with the first eruptions beneath the Amaro province of southern Ethiopia (Ebinger et al., 1993; Rooney, 2017; Rooney et al., 2014). The largest volcanic event was the emplacement of the Ethiopian flood basalt province, occurring 31-29 Ma (Hofmann, et al., 1997; Rooney, et al., 2012a; Ukstins et al., 2002) with sporadic volcanism continuing on the Ethiopian Plateau, including the emplacement of alkali shield volcanoes above the flood basalts (e.g. Choke and Guguftu 22 Ma (Kieffer et al., 2004)). Volcanic activity today is largely focused within ~15 km-wide and 60 km-long crustal magmatic segments at the rift axis which are oblique to the border faults and trend en-echelon along the rift (Ebinger et al., 2001; Wolfenden et al., 2004). Recent volcanism occurs off rift at Nabro volcano in Afar (Goitom et al., 2015), in the Yerer-Tullu Wellel Volcanotectonic Lineament (YTVL) (Rooney et al., 2014) and eruptive centres are present south of Lake Tana (Corti, 2009; Kieffer et al., 2004) (Figure 1). The volcanic segments in Afar and the Main Ethiopian Rift (MER) are the main focus of present day extension, while prior to the Pleistocene, extension was focussed at the border faults (Ebinger et al., 2001; Wolfenden et al., 2004, 2005).

Rifting in Afar initiated between 29 Ma (Wolfenden et al., 2004) and 26 Ma (Bosworth et al., 2005), just after the main flood basalt emplacement at 31-29 Ma (Hofmann et al., 1997; Pik et al., 1998; Wolfenden et al., 2004), while the MER started rifting later at 20 Ma in the south, and 11 Ma in the north (Kazmin et al., 1978; Wolfenden et al., 2004). Extension rates are variable with full spreading rates of ~6 mm/yr. for the MER (Birhanu et al., 2016; Jestin et al., 1994; Saria et al., 2014), 16 mm/yr. for the Gulf of Aden Rift (Jestin et al., 1994; Vigny et al., 2006) and 18 mm/yr. for the Red Sea Rift (McClusky et al., 2010; Vigny et al., 2006) (Figure

1a) The Tendaho Goba'ad discontinuity (TGD) separates the east-west directed extension in the northern-most MER from the northeast-southwest directed extension in Afar (Tesfaye et al., 2003).

Crustal thickness has been modified by rifting and volcanism, with the 35–40 km thick Somalian Plateau (Mackenzie et al., 2005; Stuart et al., 2006) and western edge of the Ethiopian Plateau (30–35 km thick, Ogden et al., 2019) considered representative of pre-rifted unmodified crust (Mackenzie et al., 2005; Ogden et al., 2019; Stuart et al., 2006). In contrast crustal thickness for the eastern part of the Ethiopian Plateau ranges from 40-45 km, and has been significantly affected by several kilometre thick magmatic addition from the flood basalt volcanism and likely associated lower crustal intrusions (Mackenzie et al., 2005; Ogden et al., 2019; Stuart et al., 2006; Wang et al., 2021). The crust beneath the rift is predominantly thinner than the plateaus at 25-35 km thick, with the exception of the southern MER, where crustal thickness ranges from 30-38 km. There is also evidence of magmatic additions to the MER crust (Hammond et al., 2011; Maguire et al., 2006; Stuart et al., 2006; Wang et al., 2021). In Afar crustal thickness ranges from <16-26 km, with the Danakil depression having the thinnest crust of the subaerial rift system (Dugda et al., 2005; Hammond et al., 2011; Lavayssière et al., 2018; Makris & Ginzburg, 1987).

Lithosphere-asthenosphere-boundary (LAB) depths have been interpreted from S-to-P receiver functions, surface wave tomography and a joint inversion between Rayleigh wave velocities and receiver functions. The LAB is thought to lie at 60-80 km depth beneath the Ethiopian Plateau; whereas within the rift the LAB is shallower, with seismic imaging suggesting that the mantle lithosphere is either very thin or non-existent (Dugda et al., 2007; Lavayssière et al., 2018; Rychert et al., 2012).

Previous tomographic studies suggest the upper mantle beneath the northern East African Rift is slower than expected for a mantle peridotite with Vs = 3.80-4.25 km/s (e.g. Chambers et al., 2019; Gallacher et al., 2016) and Vp 4–10% slower (e.g. Bastow et al., 2008, 2005; Fishwick, 2010). These velocities are significantly slower than those observed at similar depths beneath continental interiors, where shear velocities are typically >4.45 km/s (Kennett et al., 1995). Elevated mantle potential temperatures of 100–170°C are also interpreted beneath Ethiopia from petrological modelling (Armitage et al., 2015; Ferguson et al., 2013; Rooney et al., 2012b) and can fully account for off rift velocity variations between tomographic models and ak135 but not for those beneath the rift (e.g. Gallacher et al., 2016). Regional studies for both P-wave and shear velocity, find significantly slow velocities beneath the rift valley, which require a component of partial melt after accounting for variations in temperature and composition (Bastow et al., 2005; Chambers et al., 2019; Gallacher et al., 2016; Hammond, et al., 2013).

At crustal depths within the rift, P-wave studies image fast velocities which have previously been interpreted as solidified magmatic intrusions (Mackenzie et al., 2005; Maguire et al., 2006). More recently S-wave and surface wave velocity studies, which are more sensitive to fluids, observe slow velocities in the rift valley, suggesting a fluid component is present, in contrast to P-wave studies (Chambers et al., 2019; Kim et al., 2012; Korostelev et al., 2015) Consequently Vp/Vs ratios for the crust are high, and in places >2.0 (Hammond, et al., 2011). Elevated Vp/Vs values in the presence of active volcanism have been interpreted as fluids and melt beneath the rift (Dugda et al., 2005; Hammond, et al., 2011; Ogden et al., 2019; Stuart et al., 2006). Magnetotelluric surveys have imaged high conductivity bodies within the crust beneath the MER and Afar which provide further evidence for ongoing magmatic emplacement beneath the rift (Samrock et al., 2018; Whaler & Hautot, 2006). Off rift, there is similar evidence for ongoing lower crustal intrusions and magmatic activity. S-wave studies beneath parts of the Ethiopian Plateau, YTVL and Nabro detect slow velocities (Chambers et al., 2019; Kim et al., 2012) coupled with high conductivity bodies beneath the YTVL (Didana et al., 2014; Samrock et al., 2018, 2015; Whaler & Hautot, 2006). In addition, Nabro volcano in Eritrea erupted in 2011 (Goitom et al., 2015). While these studies hint at the presence of off rift partial melt, lack of instrumentation off rift mean the interpretations for the crustal and overall off rift plate structure remain unclear.

## 3.0 Methods

### 3.1 Datasets

We used data from 13 temporary seismic networks and 5 permanent stations installed between 1999 and 2017 (Figure 1a). We used the vertical component data from the broadband seismometer stations. Fifty-eight stations from 3 networks were included (ARGOS XM 2012-2014, Plateau YY 2014-2016 and Afar0911 2H 2012-2013), in addition to the 170 used in Chambers et al. (2019) and 290 in Gallacher et al. (2016) (Figure 1a). The variation in the number of stations between the two studies arise from the $3\lambda$ station separation requirement for the ambient noise cross-correlations resulting in the removal of the RiftVolc (Y6 2016–2017) network. Furthermore, networks and stations with short deployment durations such as the EAGLE phase iii network, were not included in the ambient noise.

### 3.2 Ambient Noise Phase Velocity

#### 3.2.1 Data Processing

The vertical component data was downsampled to 1Hz, normalised and whitened with a 4$^{th}$ order Butterworth bandpass filter between 0.005–0.4 Hz following the method of Bensen et al. (2007). The data were cross-correlated on the 24-hour long waveforms for each concurrently running station pair. The cross-correlograms for every day and each station pair were then stacked to improve the signal to noise ratio (SNR). Station pairs with less than 10 days of continuous recording, 10 days' worth of stacked cross-correlation functions, interstation distances <3$\lambda$ or a SNR <3 were removed (Bensen et al., 2007; Chambers et al., 2019; Harmon et al., 2007) resulting in 6716 cross-correlation functions (Supplementary Figure S1). We examined the stability of the cross-correlations through time, and found that typically >1 month stacks produced waveforms with phases that were within 1-2 s of the long term stack. SNR increased as expected with longer time period stacks and is consistent with numerous previous studies (e.g. Bensen et al., 2007). Then the fundamental mode Rayleigh wave data were windowed using a time variable filter (Landisman et al., 1969), and the Fourier amplitude and phase calculated at each frequency of interest via a fast Fourier transform.

#### 3.2.2 1-D Phase Velocity

The phase velocity dispersion across the region was estimated using a spatial domain technique across the entire array. A zero order Bessel function of the first kind was fitted to the real part of the Noise Correlation Function (NCF) in the Fourier domain by searching over phase velocities from 2.5–5 km/s in 0.01 km/s steps for every period of interest. For each stacked NCF the phase was measured at each period by unwrapping the phase, using the average phase velocity curve at the longest periods, to resolve cycle ambiguity (Bensen et al., 2007; Harmon et al., 2008).

#### 3.2.3 2-D Phase Velocity

The phase velocity maps were then generated by inverting the phase data using the Born approximation 2-D phase sensitivity kernels (Zhou et al., 2004) and an iterative damped least squares approach (Tarantola & Valette, 1982). We used a regular 0.25° x 0.25° grid of nodes as our parameterization for the inversion (Figure 2) and averaged the sensitivity kernel between each station pair onto the nodes (Harmon et al., 2013; Yang, Y. & Forsyth, 2006). The sensitivity kernel is calculated at every period for each station pair on a densely sampled grid (0.1° x 0.1°) and then the Gaussian distance-weighted average value is taken to determine the value at each node on the coarser grid with a Gaussian width (2-sigma) of 40 km. The inversion estimates the average phase velocity at each node, then we "undo" the Gaussian weighted average to recover a 0.1° x 0.1° sampled grid by determining the Gaussian weighted contribution of the nearest nodes to each pixel using the same 40 km Gaussian width. We present the formal error from the last iteration of the inversion, which is propagated from the nodal parameterization to the higher density grid using the Gaussian weights of each node at each pixel using the full covariance matrix. We used an a priori damping parameter of 0.2 km/s in the phase velocity inversion. This value choice stabilises the inversion but is not restrictive as the value is much larger than the standard deviations from the mean velocity at each period (Forsyth & Li, 2005). Choices smaller than 0.2 km/s resulted in damped velocity variations. This resulted in well resolved phase velocity maps between 8-26 s varying between ±0.02–0.07 km/s which are indicated in the average 1D profiles in Figure 3 and S3, with lower errors in the rift and at shallower depths.

## 3.3 Teleseismic Rayleigh wave phase velocity

### 3.3.1 Data Processing

We extracted amplitude and phase information from vertical component seismograms for earthquakes with >5.5 magnitude and epicentral distances of 25-150° (1053 events, Figure 1 inset and supplementary Figure S1). For each teleseismic event, data were processed in the following way. The raw data were demeaned and detrended and their instrument response was removed. The data was then bandpass filtered using a 4$^{th}$ order Butterworth filter between 0.005–0.4 Hz. Then the fundamental mode Rayleigh wave data were windowed using a time variable filter (Landisman et al., 1969), and the Fourier amplitude and phase calculated at each frequency of interest via a fast Fourier transform.

**3.3.2 1-D phase velocity inversion.**

We determined the average dispersion curve for the area using a 1-D version of the two-plane wave inversion method (Forsyth et al., 2005). The inversion was completed in two steps, with the first stage utilising a simulated annealing method to fit the two plane wave parameters for each event, while trying a range of starting phase velocities for the model between 3.00-4.40 km/s (Press et al., 1992). This ensured a global starting model was found for input into the second stage which utilised an iterative damped least squares inversion (Tarantola et al., 1982) (Figure 3). The inversion simultaneously solves for the phase velocity, azimuthal anisotropy and wave parameters for each event.

**3.3.3 2-D phase velocity inversion.**

We used the two plane wave method of Forsyth & Li (2005) at each period to invert for a phase velocity map using the amplitude and phase measurements described above from the teleseismic events, using 2-D finite frequency kernels (Yang & Forsyth 2006; Zhou et al., 2004). We used the same nodal parameterization as used in the ambient noise tomography, i.e., a 0.25° x 0.25° nodal grid with the outermost row and column spaced at 1° to absorb velocity heterogeneities outside the target region (Figure 2). The average 1-D phase velocity described in the previous paragraph is used as our starting model at each period. The phase velocity inversion used 2-D finite frequency kernels (Forsyth et al., 2005; Nishida, 2011; Tromp et al., 2010; Yang et al., 2006) and an iterative damped least squares approach (Tarantola & Valette 1982), which solves for phase velocities at each node, and the plane wave parameters for each event. We use the same Gaussian averaging scheme described above to generate higher resolution phase velocity grids at 0.1 x 0.1°. The phase velocity at the nodes represent an average phase over the smoothed area around the node, so the final phase velocity maps at 0.1 x 0.1° resolution are determined from the Gaussian distance weighted contributions of the nearest nodes to each pixel. We present the formal error from the last iteration of the inversion, which is propagated from the nodal parameterization to the higher density grid using the Gaussian weights of each node at each pixel using the full covariance matrix. The inversion is run twice. After the first set of inversions, events with phase misfits of >4 s are removed from the starting dataset and this is the input used for the final set of inversions. The removal of these poorly fit events is necessary as it removes waveforms with complicated source radiation patterns and other effects not accounted for in the inversion.

### 3.4 Joint Inversion for Shear Velocities

For the shear velocity inversion, we inverted each pixel of the phase velocity maps across all periods for a 1-D shear velocity structure at every node as a function of depth (Figure 3). The combined 1-D shear velocities at every pixel collectively form the 3-D volume. We used the phase velocity maps from the ambient noise for 8–26 s and the phase velocity maps from the teleseismic results for 29–100 s. The transition at 26 s from one data-type to another is chosen based on the relative amounts of data, i.e. where the teleseismic has a greater number of ray paths. Where the ambient noise and teleseismic phase velocity maps overlap, they are within error of each other, e.g. at 20–33 s (Figure S2).

We used an iterative damped least squares inversion (Tarantola & Valette 1982) and parameterised the shear velocity every 5 km vertically with 0.1° x 0.1° pixel size. The partial derivatives that relate variations in shear velocity to changes in phase velocity were calculated using DISPER80 (Saito, 1988).We assigned a nominal a priori standard error of 0.2 km/s for the shear velocity starting model and fixed the Vp/Vs ratio to 1.8, which is the crustal average from receiver function analyses (Hammond, et al., 2011; Stuart et al., 2006) and also a typical mantle value (Dziewonski, A. M. & Anderson, 1981). Variations in the choice of Vp/Vs (1.5–2.1 the observed Vp/Vs ratios in this area) produced results within error and we present the formal error from the inversion in Figure 3. Finally, we interpolated the velocity structure to 1 km depth for presentation purposes using a linear interpolation.

## 4.0 Errors and resolution

To examine the resolution of the phase velocity tomography, we produced checkerboard resolution tests (Figure 4) and synthetic structure recovery tests (Figure 5). Checkerboard tests were produced at lateral length scales of 70 km (periods 8–40 s), and 165 km (~1.5°, periods 8–100 s)(See supplementary S4 and S5 for further checkerboard tests at length scales of 110 km (1°) and 220 km (2°)). We show the checkerboards at the shortest and longest periods for the ambient noise (8 and 26 s) and teleseisms (29 and 100 s). In the period range where the two data sources overlap, the teleseisms offer improved resolution at periods longer than 29s, without losing resolution for crustal structure provided by the ambient noise. We also mask results outside the 2σ standard error contour from the phase velocity inversion. This is the formal error of the inversion from the linearized iterative least squares at the last iteration. Errors are propagated to the higher density grid in a similar fashion to the phase velocities.

The checkerboard tests indicate that 70 km length scale anomalies are well recovered for 8–40 s period, and 165 km length scale anomalies are resolved for all periods within the 2σ error contour (Figure 4). Inside the rift, anomalies are resolved at 70 km length scales for 8–40 s period, and 110 km anomaly length scale anomalies can be resolved using periods of less than 71s (Figure S4). These periods are reflective of crustal and mantle depths which are discussed here down to ~120 km depth (Figure S4). Off rift, 70 km length scale anomalies are well resolved at periods less than 17s for the ambient noise and at periods less than 40 s from the teleseisms. The 110 km length scales anomalies off rift (Figure S4), can resolve anomalies at periods less than 71s. The 165 km length scale anomalies for all periods, both on and off rift, are well resolved, however amplitude decreases at the longer periods. For checker anomaly length scales of 220 km, features are resolved at periods up to 100s (Figure S5). The decrease in amplitude recovery is likely related to the broad sensitivity kernels for the longest periods (first Fresnel zone ~500-1000 km wide for 100s period (Yoshizawa & Kennett, 2002)) and fewer ray paths. In areas where ray coverage is sparse we have poorer resolution, such as the Red Sea, Gulf of Aden and eastern part of Afar. There is also northeast-southwest smearing of the checkerboards beneath the Red Sea Rift and northwest-southeast smearing beneath Yemen. Consequently, we do not interpret these areas.

In the synthetic recovery tests, we input a slow velocity anomaly of similar magnitude to our output models in the MER and beneath the Ethiopian Plateau. Broadly, based on depth sensitivity kernels (Figure 3), features >70 km in length scale are well resolved in the upper 70 km and features >150 km in length are resolvable at all depths of the shear velocity model. We show periods at the minimum and maximum period for the ANT (8 and 26s) and teleseisms (29 and 100s) to show the full range of recovery (Figure 5). Within the rift, the recovery tests indicate phase velocity variations are resolved in our models at all periods (Figure 5) though at periods >71 s the anomaly beneath the rift is less elongate and focusses to the northwest of the MER. Off rift synthetic recovery tests at periods <29s, indicate the two slow velocity features are resolvable if they are >70 km wide. At longer periods the two anomalies are no longer distinct. Synthetic recovery tests within the Red Sea and Gulf of Aden Rifts suggest there is smearing in a northeast direction particularly for the Gulf of Aden at longer periods.

To examine vertical resolution, we perform a spike test (Backus & Gilbert, 1970) for a range of model depths (Figure 6). These kernels show the recovery of a spike function based on the diagonals of the formal resolution matrix. The formal resolution matrix is derived from the damped least squares inversion where the Resolution:

$\boldsymbol{R} = \left(\boldsymbol{G}^{\boldsymbol{T}} \boldsymbol{C}_{\boldsymbol{nn}}{}^{-\boldsymbol{1}} \boldsymbol{G} + \boldsymbol{C}_{\boldsymbol{mm}}\right)^{-\boldsymbol{1}} \left(\boldsymbol{G}^{\boldsymbol{T}} \boldsymbol{C}_{\boldsymbol{nn}}{}^{-\boldsymbol{1}} \boldsymbol{G}\right)$. $\boldsymbol{G}$ is the matrix of partial derivatives from the kernel at each node, $\boldsymbol{C}_{\boldsymbol{nn}}$ is the data covariance matrix and $\boldsymbol{C}_{\boldsymbol{mm}}$ is the model covariance matrix (Saito, 1988). Resolution ranges between 0-1, where 1 indicates a completely resolved model parameter (e.g. velocity of a layer) and 0 means not resolved. A value of 0.33 would require 3 adjacent layers to resolve 1 piece of independent information about velocity. The kernels suggest shear velocities are resolvable down to 150 km depth (Figure 3 and Figure 6) after which the resolution starts to deviate from the typical bell curve shape. At the shallowest depths (7-22 km), depth slices averaged over ±10 km are resolved, and for the deepest slices at 142-162 km depth are resolved when averaged over ±50 km velocity averages.

## <u>5.0 Results</u>

### 5.1 1-D dispersion curves and shear velocity model

Average 1-D dispersion curves measured from the ambient noise and teleseismic data are shown in Figure 3. Phase velocities range from 2.93 ± 0.02 km/s at 8s to 3.87 ± 0.03 km/s at 100s (Figure 3 and Figure 7). Where the phase velocities from the ambient noise and teleseisms overlap (20-33 s) (Figure S2), the velocities are similar to one another and within the standard error. The shear velocity structure is displayed in Figure 3b with shear velocities ranging from 3.10 ± 0.02 km/s at 5 km depth to 4.42 ± 0.03 km/s at 150 km depth. The average 1-D shear velocities are slower than the input model (green line) at most depths except from 40-80 km depth. In Figure 3c we present the sensitivity kernels, which indicate the depths of peak sensitivity for the shear velocity inversion at 8, 15, 20, 26, 29, 40, 71 and 100 s period. The kernels suggest 150 km depth is the limit of our sensitivity.

### 5.2 2-D Phase Velocities

We generate phase velocity maps from 8-100 s (Figure 7) and observe velocity variations that correlate with geologic and tectonic features. Phase velocities are more variable at shorter periods ranging from 2.85-3.45 ±0.04 km/s at 10 s becoming less laterally variable at 100 s period (3.80-3.90 ±0.06 km/s).

Within the rift system, the MER is the slowest region of our study for all periods (at 10s the Red Sea is slower but due to ray path bias, we do not interpret this region). We observe minimum velocities ranging from 2.90 ±0.03 km/s at 10 s to 3.82 ±0.04 km/s at 100 s period. Beneath Afar, velocities are ~0.20 km/s faster than the MER at all periods. Phase velocity ranges from 3.15 ±0.03 km/s at 10 s to 3.90 ±0.04 km/s at 100 s period. Within the rifts, slow velocities are not laterally continuous and at periods <71 s, display segmentation. The anomalies are ~100 km in length and in most cases broadly correlate with Quaternary volcanism or hydrothermal sites.

The velocity structure on the Ethiopian Plateau is variable, exhibiting both fast and slow velocity regions across the period range of interest. The eastern part of the Ethiopian Plateau is slow at short periods (from 8 to 26 s) with velocities of 3.00 ±0.04 km/s at 10 s to 3.50 ±0.05 km/s at 26 s period. At 20 to 26 s period, the shape of the two slow velocity regions connect which may in part be due to smearing according to our resolution tests (Figure 5). At longer periods (>29 s period), phase velocities beneath the eastern part of the Ethiopian Plateau are similar to background phase velocity values (~3.80-3.90 ±0.05 km/s). In contrast, the western part of the Ethiopian Plateau is the fastest area of our study at all periods with phase velocities of 3.35 ±0.04 km/s at 10 s period increasing to 3.92 ±0.05 km/s at 100 s depth.

**5.3 3-D Shear Velocity Structure**

At lithospheric depths (10-80 km), we observe strong lateral variations in shear velocity, up to 0.85 km/s across our study region, which likely reflect a combination of significant changes in crustal thickness and variability in mantle structure. Figure 8 and Figure 9 show depth slices and cross-sections through the shear velocity model, respectively. The slowest velocities in the region are beneath the MER from 10–50 km depth and the Danakil depression from 50-80 km depth (due to variations in lithospheric thickness). For instance, at crustal depths (10 km) we find Vs = 3.00 ±0.03 km/s and at mantle depths (60 km) we find Vs = 4.05 ±0.03 km/s (Figure 8 a-c). In profile A–A' (Figure 9a) south of the MER, there is a fast lid visible between 37–38.5° E at 60–80 km depth. Within the rift, this fast lid is broken by slow velocity anomalies before becoming prevalent again near the Arabian Peninsula.

At 20-40 km depth there is a slow velocity region centred ~100 km southeast of Lake Tana beneath the eastern part of the Ethiopian Plateau (3.10-3.85 ±0.04 km/s at depths of 10 to 40 km respectively), and another anomaly ~100 east of this anomaly centred beneath the border fault region. These anomalies are not present below 60 km depth (Figure 8c).

The western Ethiopian Plateau is one of the fastest regions at 20-40 km depths with velocities >3.80 km/s at 20 km and >4.15 km/s at 40 km (±0.04 km/s), but is close to the average velocity across the region at 60 km. Profile B-B' (Figure 9b) shows there is a high velocity lid (velocity >4.15 km/s), from 60-80 km depth west of the rift (<38.5° E), and to the east of the rift (>40°

E). We note that this study is the first to obtain shear wave velocities this far west on the Ethiopian Plateau due to the addition of recent seismic networks (Figure 1).

Afar has some of the fastest velocities in the region at 20 km depth ( ~3.80 km/s/0, which likely reflects the thinner crust in this region compared to the Plateau. At 40-60 km depth, the Afar region is characterised by several punctuated slow velocity regions with velocities <3.9 km/s, which are coincident with regions of active hydrothermal sites (stars in Figure 8) or recent volcanism (red polygons in Figure 8). Specifically, beneath the crustal magmatic segments and along the TGD (shown in Figure 1 as red polygons and dashed line respectively) the velocities are ~0.2 km/s slower than the rest of Afar at all lithospheric depths.

At asthenospheric depths (>60 km in Afar and >80 km in the MER and Plateau), we also observe several punctuated slow velocity regions. Specifically, in the 80-120 km depth range, the region beneath the MER is the slowest in the region with velocities <4.15 km/s (Figure 8 and S6). The slow velocity anomaly is not centred beneath the rift but is offset towards the west, beneath Addis Ababa and straddling the rift. There are two other slow velocity regions with velocities <4.15 km/s located near the Red Sea and the Gulf of Aden. Within Afar, in this depth range, the slow velocities are not as strong.

The slow velocity anomalies within the rift appear to systematically extend to shallower depths going from the MER northwards. Profile A-A’, along the MER rift axis (Figure 9a), extending into Afar, shows the relationship between the slow velocity anomalies. Near the MER, the slow velocities are visible beneath the fast lid, extending from 80-120 km depth using the 4.05 km/s contour (Figure 9a). Going northwards, the slow velocity anomalies are centred at shallower depths going to 75 km and then to 65 km depth beneath Afar. The base of the anomalies appears fairly constant at ~120 km depth. There does not appear to be much variation in structure at greater depths in our models though this is close to the limits of our depth resolution.

The strongest anomalies at crustal depths within the MER and the Ethiopian Plateau, are displaced from the strongest anomalies in the asthenosphere, while in Afar the anomalies in the asthenosphere are close to regions of geologically recent volcanism. In the MER the slow velocities at 20 km depth are located ~100 km southwest of the slowest velocities in the asthenosphere. Beneath the Ethiopian Plateau, velocities at asthenospheric depths are faster than those within the MER and the slowest asthenospheric velocities that may link to those within the crust off rift, are again located within the asthenosphere beneath the MER. Beneath Afar, the slow velocity regions are predominantly located beneath the locations of active hydrothermal sites (stars Figure 8) and recent volcanos (red triangles Figure 8).

## 6.0 Interpretation

Our results are the first absolute seismic velocity model for the crust and upper mantle beneath both the rift and the Ethiopian Plateau. The primary new components are the crustal structure beneath the Ethiopian Plateau and significant improvement in the resolution of upper mantle depths from the joint inversion. The crustal structure beneath the rift is broadly consistent to that described in Chambers et al. (2019) due to similar methods and networks used. The addition of the Ethiopian Plateau network has provided additional data that have been used to provide fundamental new constraints of the absolute shear velocity structure of the crust and upper mantle off rift beneath the Ethiopian Plateau and beneath parts of the Somalian Plateau. Below we summarize the previous findings for the crustal and uppermost mantle structure from Chambers et al. (2019) and then focus on the new results off rift beneath the Ethiopian Plateau.

We then discuss mantle depths beneath the area, where we have significantly improved resolution from the joint inversion.

### 6.1 Crustal Structure

At shallow depths (10-40 km) we observe the largest range in shear velocity. This has been observed in previous tomographic studies which attributed the range to changes in crustal thickness, melt and temperature (Chambers et al., 2019; Hammond, 2014; Kim et al., 2012; Korostelev et al., 2015). Within the MER observed velocities are slow and have been attributed to higher temperatures and/or the presence of partial melt in the crust. Beneath Afar, where slow velocities are observed beneath crustal magmatic segments in our model (>0.2 km/s slower than surroundings, Vs = 3.50 ±0.02 km/s) ), a similar interpretation has been made for the origin of the slow velocities (e.g. Chambers et al., 2019; Rooney, 2020b) (Figure 8). Temperatures in the crust would be too high to account for the observed velocity variations making partial melt the most likely explanation. The amount of partial melt required to explain the slowest velocities ranges from 0.5 to 4% (Chambers et al., 2019). Variations in crustal thickness are also thought to have a control on the observed velocities as thicker crust can increase melt residence times resulting in more felsic compositions and a deep crustal melt zone (Annen et al., 2006; Karakas & Dufek, 2015; Siegburg et al., 2018). The faster velocities in Afar at 20–40 km depth (3.80–4.05 ±0.02 km/s), are consistent with slower than average mantle velocities constrained in previous studies (~3.8-4.1 km/s) (e.g. Bastow et al., 2008; Gallacher et al., 2016).

In contrast to other studies, we provide the first shear velocity model for the Ethiopian Plateau allowing the first seismic interpretation of the velocity structure away from the rift. We observe slow anomalies off rift southeast of Lake Tana on the eastern part of the Ethiopian Plateau (3.10-3.85 ±0.04 km/s at depths of 10 to 40 km). At mid to lower crustal depths, and periods >15s, synthetic recovery tests suggest there is smearing between the two slow velocity anomalies, and with those in the MER (Figure 5). We do not observe a slow velocity anomaly beneath the Ethiopian Plateau below 40 km depth which could be a result of features being too small to be resolved, are isolated to the crust, or finally, are at the limit of our well resolved region off rift. The slow velocity anomalies are a similar magnitude to those within the MER, and broadly correlate in map view to known geothermal activity and past volcanism (Figure 8). The last major volcanic event on the Ethiopian Plateau was >21 Myrs (Rooney, 2017) though there is evidence for limited quaternary activity along the YTVL and southwest of lake Tana (Kieffer et al., 2004; Meshesha & Shinjo, 2007). It is therefore unlikely that a remnant thermal anomaly could explain our observations (Figure S7), as simple conductive cooling calculations indicate that a 1300°C thermal anomaly would dissipate in <10 Myr. We suggest there has been further recent magmatic emplacement.

The western part of the Ethiopian Plateau is one of the seismically fastest areas of this study (in contrast to the East), and is located 250-500 kms from the rift, providing us with information about pre-rift structure. The distance from the rift coupled with geological studies (e.g. Jones, (1976); Rooney, (2019)) suggests the western part of the Ethiopian Plateau has been minimally impacted by rifting processes. In addition there is little evidence for significant flood basalt magmatism (Mège et al., 2004). We interpret the velocity observations as being most similar to original plate structure before rifting, with our inferred crustal thickness between 20–30 km thick (using the 3.60 km/s contour as used in Chambers et al., (2019)). Ogden et al. (2019), performed receiver function analysis in the same area, finding crustal thicknesses of ~30 km at the western edge of the Ethiopian Plateau and interpreted the area as being unaffected by lower crustal intrusion from the Oligocene flood basalts or younger rifting, consistent with our observations.

### 6.2 Lithospheric Mantle Structure

In the upper mantle we observe a fast lid in 1-D profile (Figure 3) and cross-sections (Figure 9) that are >0.1 km/s faster than the surroundings. We note that while fast, the velocities are slower than lithospheric mantle observed in other continental settings (maximum of 4.30 ±0.05 km/s for our model in comparison to 4.45 km/s for ak135) (Kennett et al., 1995). This feature is broadly at 60–80 km depth off rift, but is absent beneath Afar. In the MER the velocities we observe at similar depths alternate between slow and fast, part way between fast velocities observed off rift and the absence in Afar. The base of the fast lid is commonly associated with the lithosphere-asthenosphere-boundary (LAB) (Fishwick, 2010; Lavayssière et al., 2018; Rychert et al., 2012, 2005) and we therefore plot the S-to-P LAB results of Lavayssière et al. (2018) on our cross-sections (Figure 9 red diamonds in lower panels). We find good agreement between the locations of our fastest velocities (Vs >4.15 km/s) and the existence of a strong LAB phase from the S-to-P results suggesting we are imaging a similar feature. The fast lid is most prominent off rift beneath the rift flanks and Ethiopian Plateau in Profile B-B' (Figure 9b), in regions less affected by rifting. In the rift Profile A-A' which extends from the southern MER to the Arabian Peninsula (Figure 9a), a weaker fast velocity zone (Vs = 4.1-4.15 km/s) is intermittently visible within the rift and is underlain by the slowest asthenospheric velocities (discussed in the next section). The fast lid becomes prevalent again near the Arabian Peninsula. Our result, with no discernible fast lid in Afar, is consistent with S-to-P results which also did not find a strong, significant LAB phase beneath the majority of the rift (Lavayssière et al., 2018; Rychert et al., 2012). The presence of the slowest asthenospheric velocities (3.98-4.06 ±0.03 km/s) beneath areas where receiver functions do not detect a significant LAB phase

(Lavayssière et al., 2018; Rychert et al., 2012), is consistent with a lack of a fast lid in these regions, possibly caused by partial melt at shallow depths (10-60 km depth).

### 6.3 Asthenospheric Anomalies

At asthenospheric depths of ~80 km beneath the Ethiopian Plateau we observe velocities of 4.20 ±0.05 km/s, which is lower than the global average for continents at that depth (4.45 km/s) using ak135 (Gallacher et al., 2016; Kennett et al., 1995) (Figure 3b and Figure 8). Similar velocity structure imaged in the asthenosphere beneath the Ethiopian Plateau has been explained with elevated temperatures of 100–170°C (e.g. Gallacher et al., 2016), consistent with petrological constraints of the regional mantle potential temperature (Armitage et al., 2015; Ferguson et al., 2013; Rooney et al., 2012b). These velocities provide the regional background velocity for the asthenosphere without melt for comparison to the sub-rift structure. Melt may not necessarily be required for this modest velocity anomaly at least over the broad depth ranges (~40 km) and lateral areas (>160 km) resolvable by surface waves in this region. However, receiver functions image a strong, sharp discontinuity beneath the Ethiopian Plateau (Lavayssière et al., 2018; Rychert et al., 2012) that likely requires a small amount of partial melt, indicating it may exist in a more limited depth and/or lateral area.

We observe slow velocity anomalies (Vs <4.05 km/s) at asthenospheric depths of > 60 km within the rifts, which are punctuated segments that are ~110x80 km wide, spaced ~70 km apart, and have a base at ~120 km depth. The segments we describe do not correlate to the surface expressions of magmatic segments described in crustal studies. The slow velocity anomalies get progressively shallower, slower and broader in lateral extent northwards, towards areas at more advanced stages of rifting (Figure 9a). The slowest and largest anomaly with the shallowest starting depth (60 km) exists beneath Afar, the region in the latest stage of rifting (9% velocity decrease when comparing the segments to the rift flanks), while for the MER the shallowest starting depth for the slow velocity bodies are ~80 km depth. We note that while the anomalies themselves are well-resolved, absolute depths could vary by 20-30 km given our sensitivity at these depths. Mantle potential temperatures in the rift are only moderately elevated, ~1450°C (Ferguson et al., 2013; Petersen et al., 2015; Rooney, Herzberg, et al., 2012) based on geochemical observations. With this temperature, we would expect velocities to be reduced by ~3% using a Burgers model (Jackson & Faul, 2010) for a peridotite mantle and an estimated geotherm for the MER (Chambers et al., 2019). Composition and temperature are therefore not sufficient to account for the velocity reduction, which suggests a fluid component is required in the asthenosphere beneath the rift. We postulate the fluid component is most likely partial melt, from the abundance of Quaternary volcanism at the surface, which is in agreement with previous tomographic studies (Bastow et al., 2008; Chambers et al., 2019; Gallacher et al., 2016). The anomalies occur at depths consistent with previous geochemical estimates of melt generation (53–120 km depth) (Ferguson et al., 2013; Rooney et al., 2005).

The slow velocity segments in the asthenosphere (Figure 9a), are present at the earliest stages of rifting beneath areas where the crust and lithosphere is not significantly thinner than beneath the Ethiopian Plateau (40 km thick crust and 80 km thick lithosphere (Lavayssière et al., 2018; Stuart et al., 2006)). Furthermore the segments persist into areas of later stage rifting in the northern section of A-A' in Afar (Figure 9a) where the crust is thinner (crustal thicknesses of 22 km (Hammond, et al., 2011)). These observations suggest segmented melt supply starts prior to significant crustal and plate thinning.

Segmentation beneath rifts is not isolated to this study and has been observed beneath more mature rifts and mid ocean ridges (e.g. Gulf of California, Red Sea Rift, the Mid Atlantic Ridge (Harmon et al., 2020; Lekic et al., 2011; Ligi et al., 2012; Wang et al., 2009) and also beneath the EAR in the same region as our study (Civiero et al., 2015, 2019; Gallacher et al., 2016). The processes generating segmentation beneath the EAR are debated (e.g. Bastow et al., 2008;

Civiero et al., 2015; Gallacher et al., 2016; Ligi et al., 2012). The 2 main hypotheses for segmentation are decompression melting with buoyancy driven upwelling from the release of melt (e.g. Gallacher et al., 2016) or the presence of mantle plumelets (e.g. Civiero et al., 2019). The spatial correlation of our anomalies within the rift coupled with larger, slower and shallowing of the top of the slow velocity anomalies towards more advanced stages of rifting, favours rift related buoyancy driven upwelling.

Off rift beneath the Ethiopian Plateau at crustal depths, we observed velocities slow enough to contain melt (Figure 9). However velocities in the asthenosphere can be accounted for by temperature alone at scales resolvable by surface waves (e.g. Gallacher et al., 2016). To explain the disconnect between slow velocities off rift in the crust, and limited evidence for melt production in the asthenosphere off rift we propose 3 possibilities. 1. Melt is present off rift (Civiero et al., 2015) but is localised in pockets that are below our resolving power, 2. Melt is ephemeral and was previously located off rift but has now been drained (Sim et al., 2020) and 3. Melt has laterally migrated from the rift axis along permeability boundaries (Sparks & Parmentier, 1991). The first option is sugggestive of ponding beneath a permeability barrier, and therefore likely also includes migration and/or ephemeral character, and therefore we proceed discussing the latter two options. Similar observations of disconnected slow velocity anomalies have been observed in previous studies at more developed rifts or ridges, which hypothesise lateral melt migration is occuring along a permeability boundary (Braun & Sohn, 2003; Ghods & Arkani-Hamed, 2000; Harmon et al., 2020; Holtzman & Kendall, 2010; Rychert et al., 2020; Varga et al., 2008; Wang et al., 2020) and/or melt is ephemeral (Harmon et al., 2020; Rychert et al., 2020; Wang et al., 2020). Within the MER we also observe the slowest velocity anomalies at asthenospheric depths in our model, are not located directly beneath the slowest crustal velocity anomalies (Figure 9). In line with previous studies (Braun et al., 2003; Gallacher et al., 2016; Ghods et al., 2000; Holtzman & Kendall, 2010) we suggest the most likely explanation for the disconnect between melt in the asthenosphere and melt in the crust within the rift, is likely due to lateral melt migration along permeability boundaries in the lithosphere. Overall, this study suggests melt generation and migration are dynamic processes, which require further study to fully understand rifting processes and the factors that dictate the locations of active volcanic/hydrothermal regions.

## 7.0 Conclusions

We present the results from a joint inversion of ambient noise and teleseismic Rayleigh waves to produce a 3-D absolute shear velocity map from 10-150 km depth, for the northern East African Rift. At crustal depths we observe significant lateral velocity variations which can partly be explained by variations in crustal thickness. At crustal depths velocities are slowest beneath the Main Ethiopian Rift and the eastern part of the Ethiopian Plateau and are slow enough to require a component of partial melt. A fast lid, consistent with previous measurements for the Lithosphere-Asthenosphere-Boundary, is observed at 60–80 km depth off rift (>0.1 km/s faster than surroundings). However, within the rift, the fast lid is obscured where it is underlain by asthenospheric segmented slow velocity anomalies, which we interpret as melt infiltration to shallow depths. At asthenospheric depths beneath the Ethiopian Plateau we observe velocities only slightly slower (4.30 ±0.05 km/s) than global models, that can be explained by elevated temperatures. The rift is significantly slower than off rift at asthenospheric depths, and we observe segmented slow velocity anomalies at 60-120 km depth, including in areas that have not undergone significant crustal and plate thinning. The asthenospheric slow velocity segments are interpreted as areas of partial melt and suggest segmented melt supply starts prior to significant crustal and plate thinning. Furthermore, asthenospheric anomalies are not directly beneath the melt-rich crustal regions, including those off rift, suggesting melt laterally migrates within the mantle, and/or melt is ephemeral and the mantle source for the anomalies observed at crustal depths, have been drained.

**Acknowledgments**

E.L.C acknowledges funding from NERC studentship NE/L002531/1. C.A.R. and N.H. acknowledge funding from NERC grants NE/M003507/1 and NE/K010654/1 and ERC grant GA 638665. D.K. is supported by NERC grant NE/L013932 and by MiUR through PRIN grant 2017P9AT72. We thank SEIS-UK (supported by NERC under agreement R8/H10/64.F) for use of instruments and computing facilities. Some figures were made using GMT (Wessel et al. 2013).

**Data Availability Statement**

All data used to generate the models are freely available from the IRIS Data Management Center (IRISDMC; https://service.iris.edu/fdsnws/dataselect/1/) funded through SAGE Proposal of the NSF under Cooperative Agreement EAR-126168. The networks used are: RiftVolc Y6 (https://doi.org/10.7914/SN/Y6_2016), ARGOS XM (https://doi.org/10.7914/SN/XM_2012), Plateau YY (https://doi.org/10.7914/SN/YY_2013), EKBSE XI (https://doi.org/10.7914/SN/XI_2000), YOCMAL XW( https://doi.org/10.7914/SN/XW_2009), EAGLE geophysical XJ (https://www.fdsn.org/networks/detail/XJ_2002/), EAGLE geoscientific YJ (https://www.fdsn.org/networks/detail/YJ_2001/), Boina YZ (https://www.fdsn.org/networks/detail/YZ_2005/), AFAR07 ZE (https://doi.org/10.7914/SN/ZE_2007), Afar depression ZK (https://doi.org/10.7914/SN/ZK_2009), Africa Array AF (https://doi.org/10.7914/SN/AF), IU (https://doi.org/10.7914/SN/IU), GEOFON GE (https://doi.org/10.14470/TR560404), Eritrea YR/5H (https://doi.org/10.7914/SN/5H_2011), Danakil depression ZR/2H (https://doi.org/10.7914/SN/2H_2009), GEOSCOPE G (https://doi.org/10.18715/GEOSCOPE.G).

## References


Annen, C., Blundy, J. D., & Sparks, R. S. J. (2006). The genesis of intermediate and silicic magmas in deep crustal hot zones. *Journal of Petrology*, *47*(3), 505–539. https://doi.org/10.1093/petrology/egi084

Armitage, J. J., Ferguson, D. J., Goes, S., Hammond, J. O. S., Calais, E., Rychert, C. A., & Harmon, N. (2015). Upper mantle temperature and the onset of extension and break-up in Afar, Africa. *Earth and Planetary Science Letters*, *418*, 78–90. https://doi.org/10.1016/j.epsl.2015.02.039

Backus, G. E., & Gilbert, F. (1970). Uniqueness in the inversion of inaccurate gross Earth data. *Philosophical Transactions of the Royal Society of London. Series A, Mathematical and Physical Sciences*, *266*, 123–192.

Barberi, F., Tazieff, H., & Varet, J. (1972). Volcanism in the Afar Depression: Its Tectonic and Magmatic Significance. *Developments in Geotectonics*, *7*(C), 19–29. https://doi.org/10.1016/B978-0-444-41087-0.50007-5

Bastow, I. D., Nyblade, A. A., Stuart, G. W., Rooney, T. O., & Benoit, M. H. (2008). Upper mantle seismic structure beneath the Ethiopian hot spot: Rifting at the edge of the African low-velocity anomaly. *Geochemistry, Geophysics, Geosystems*, *9*(12). https://doi.org/10.1029/2008GC002107

Bastow, I. D., Stuart, G. W., Kendall, J.-M., & Ebinger, C. J. (2005). Upper-mantle seismic structure in a region of incipient continental breakup: Northern Ethiopian rift. *Geophysical Journal International*, *162*(2), 479–493. https://doi.org/10.1111/j.1365-246X.2005.02666.x

Bensen, G. D., Ritzwoller, M. H., Barmin, M. P., Levshin, A. L., Lin, F.-C., Moschetti, M.

P., … Yang, Y. (2007). Processing seismic ambient noise data to obtain reliable broad-band surface wave dispersion measurements. *Geophysical Journal International*, *169*(3), 1239–1260. https://doi.org/10.1111/j.1365-246X.2007.03374.x

Birhanu, Y., Bendick, R., Fisseha, S., Lewi, E., Floyd, M., King, R., & Reilinger, R. (2016). GPS constraints on broad scale extension in the Ethiopian Highlands and Main Ethiopian Rift. *Geophysical Research Letters*, *43*(13), 6844–6851. https://doi.org/10.1002/2016GL069890

Bosworth, W., Huchon, P., & McClay, K. (2005). The Red Sea and Gulf of Aden Basins. *Journal of African Earth Sciences*, *43*(1–3), 334–378. https://doi.org/10.1016/j.jafrearsci.2005.07.020

Braun, M. G., & Sohn, R. A. (2003). Melt migration in plume-ridge systems. *Earth and Planetary Science Letters*, *213*(3–4), 417–430. https://doi.org/10.1016/S0012-821X(03)00279-6

Buck, W. R. (2006). The role of magma in the development of the Afro-Arabian Rift System. *Geological Society, London, Special Publications*, *259*(1), 43–54. https://doi.org/10.1144/GSL.SP.2006.259.01.05

Chambers, E. L., Harmon, N., Keir, D., & Rychert, C. A. (2019). Using Ambient Noise to Image the Northern East African Rift. *Geochemistry, Geophysics, Geosystems*, *20*, 2091–2109. https://doi.org/10.1029/2018GC008129

Civiero, C., Armitage, J. J., Goes, S., & Hammond, J. O. S. (2019). The Seismic Signature of Upper-Mantle Plumes: Application to the Northern East African Rift. *Geochemistry, Geophysics, Geosystems*, 1–17. https://doi.org/10.1029/2019GC008636

Civiero, C., Hammond, J. O. S., Goes, S., Fishwick, S., Ahmed, A., Ayele, A., … Stuart, G. W. (2015). Multiple mantle upwellings in the transition zone beneath the northern East-African Rift system from relative P-wave travel-time tomography. *Geochemistry,* *Geophysics, Geosystems*, *16*(9), 2949–2968. https://doi.org/10.1002/2015GC005948

Corti, G. (2009). Continental rift evolution: From rift initiation to incipient break-up in the Main Ethiopian Rift, East Africa. *Earth-Science Reviews*, *96*(1–2), 1–53. https://doi.org/10.1016/j.earscirev.2009.06.005

Didana, Y. L., Thiel, S., & Heinson, G. (2014). Magnetotelluric imaging of upper crustal partial melt at Tendaho graben in Afar, Ethiopia. *Geophysical Research Letters*, *41*(9), 3089–3095. https://doi.org/10.1002/2014GL060000

Dugda, M. T., Nyblade, A. A., & Julia, J. (2007). Thin lithosphere beneath the Ethiopian Plateau revealed by a joint inversion of Rayleigh wave group velocities and receiver functions. *Journal of Geophysical Research: Solid Earth*, *112*(8), 1–14. https://doi.org/10.1029/2006JB004918

Dugda, M. T., Nyblade, A. A., Julia, J., Langston, C. A., Ammon, C. J., & Simiyu, S. (2005). Crustal structure in Ethiopia and Kenya from receiver function analysis : Implications for rift development in eastern Africa. *Journal of Geophysical Research*, *110*. https://doi.org/10.1029/2004JB003065

Dziewonski, A. M., & Anderson, D. L. (1981). Preliminary reference Earth model. *Physics of the Earth and Planetary Interiors*, *25*(4), 297–356. https://doi.org/10.1016/0031-9201(81)90046-7

Ebinger, C. J., & Casey, M. (2001). Continental breakup in magmatic provinces: An Ethiopian example. *Geology*, *29*(6), 527–530.

Ebinger, C. J., Yemane, T., WoldeGabriel, G., Aronson, J. L., & C., W. R. (1993). Late Eocene-Recent volcanism and faulting in the southern main Ethiopian rift. *Journal of the Geological Society London*, *150*, 99–108.

Ferguson, D. J., MacLennan, J., Bastow, I. D., Pyle, D. M., Jones, S. M., Keir, D., … Yirgu, G. (2013). Melting during late-stage rifting in Afar is hot and deep. *Nature*, *499*(7456), 70–73. https://doi.org/10.1038/nature12292

Fishwick, S. (2010). Surface wave tomography: Imaging of the lithosphere-asthenosphere boundary beneath central and southern Africa? *Lithos*, *120*(1–2), 63–73. https://doi.org/10.1016/j.lithos.2010.05.011

Forsyth, D. W., & Li, A. (2005). Array analysis of two-dimensional variations in surface wave phase velocity and azimuthal anisotropy in the presence of multipathing interference. *Seismic Earth: Array Analysis of Broadband Seismograms*, 81–97. https://doi.org/10.1029/157GM06

Furman, T., Bryce, J., Rooney, T. O., Hanan, B. B., Yirgu, G., & Ayalew, D. (2006). Heads and tails: 30 million years of the Afar plume. *Geological Society, London, Special Publications*, *259*, 95–119.

Gallacher, R. J., Keir, D., Harmon, N., Stuart, G. W., Leroy, S., Hammond, J. O. S., … Ahmed, A. (2016). The initiation of segmented buoyancy-driven melting during continental breakup. *Nature Communications*, *7*, 13110. https://doi.org/10.1038/ncomms13110

Ghods, A., & Arkani-Hamed, J. (2000). Melt migration beneath mid-ocean ridges. *Geophysical Journal International*, *140*(3), 687–697. https://doi.org/10.1046/j.1365-246X.2000.00032.x

Goitom, B., Oppenheimer, C., Hammond, J. O. S., Grandin, R., Barnie, T. D., Donovan, A., … Berhe, S. (2015). First recorded eruption of Nabro volcano, Eritrea, 2011. *Bulletin of Volcanology*, *77*(10). https://doi.org/10.1007/s00445-015-0966-3

Hammond, J. O. S. (2014). Constraining melt geometries beneath the Afar Depression, Ethiopia from teleseismic receiver functions: The anisotropic H-k stacking technique. *Geochemistry, Geophysics, Geosystems*, *15*(4), 1316–1322. https://doi.org/10.1002/2013GC005186

Hammond, J. O. S., Kendall, J.-M., Stuart, G. W., Ebinger, C. J., Bastow, I. D., Keir, D., … Wright, T. J. (2013). Mantle upwelling and initiation of rift segmentation beneath the Afar Depression. *Geology*, *41*(6), 635–638. https://doi.org/10.1130/G33925.1

Hammond, J. O. S., Kendall, J.-M., Stuart, G. W., Keir, D., Ebinger, C. J., Ayele, A., & Belachew, M. (2011). The nature of the crust beneath the Afar triple junction: Evidence from receiver functions. *Geochemistry, Geophysics, Geosystems*, *12*(12), 1–24. https://doi.org/10.1029/2011GC003738

Harmon, N., De La Cruz, M. S., Rychert, C. A., Abers, G. A., & Fischer, K. M. (2013). Crustal and mantle shear velocity structure of Costa Rica and Nicaragua from ambient noise and teleseismic Rayleigh wave tomography. *Geophysical Journal International*, *195*(2), 1300–1313. https://doi.org/10.1093/gji/ggt309

Harmon, N., Forsyth, D. W., & Webb, S. C. (2007). Using ambient seismic noise to determine short-period phase velocities and shallow shear velocities in young oceanic lithosphere. *Bulletin of the Seismological Society of America*, *97*(6), 2009–2023. https://doi.org/10.1785/0120070050

Harmon, N., Gerstoft, P., Rychert, C. A., Abers, G. A., de la Cruz, M. S., & Fischer, K. M. (2008). Phase velocities from seismic noise using beamforming and cross correlation in Costa Rica and Nicaragua. *Geophysical Research Letters*, *35*(19), 1–6. https://doi.org/10.1029/2008GL035387

Harmon, N., Rychert, C. A., Kendall, J.-M., Agius, M., Bogiatzis, P., & Tharimena, S. (2020). Evolution of the Oceanic Lithosphere in the Equatorial Atlantic From Rayleigh Wave Tomography, Evidence for Small-Scale Convection From the PI-LAB Experiment. *Geochemistry, Geophysics, Geosystems*, *21*(9). https://doi.org/10.1029/2020gc009174

Hofmann, C., Courtillot, V., Féraud, G., Rochette, P., Yirgu, G., Ketefo, E., & Pik, R. (1997).

Timing of the ethiopian flood basalt event and implications for plume birth and global change. *Nature*, *389*(6653), 838–841. https://doi.org/10.1038/39853

Holtzman, B. K., & Kendall, J.-M. (2010). Organized melt, seismic anisotropy, and plate boundary lubrication. *Geochemistry, Geophysics, Geosystems*, *11*(12), 1–29. https://doi.org/10.1029/2010GC003296

Jackson, I., & Faul, U. H. (2010). Grainsize-sensitive viscoelastic relaxation in olivine: Towards a robust laboratory-based model for seismological application. *Physics of the Earth and Planetary Interiors*, *183*(1–2), 151–163. https://doi.org/10.1016/j.pepi.2010.09.005

Jestin, F., Huchon, P., & Gaulier, J. M. (1994). The Somalia Plate and the East-African Rift System - Present- Day Kinematics. *Geophysical Journal International*, *116*(3), 637–654.

Jones, P. W. (1976). Age of the lower flood basalts of the Ethiopian plateau. *Nature*, *261*(5561), 567–569. https://doi.org/10.1038/261567a0

Karakas, O., & Dufek, J. (2015). Melt evolution and residence in extending crust: Thermal modeling of the crust and crustal magmas. *Earth and Planetary Science Letters*, *425*, 131–144. https://doi.org/10.1016/j.epsl.2015.06.001

Kazmin, V., Shifferaw, A., & Balcha, T. (1978). The Ethiopian basement: Stratigraphy and possible manner of evolution. *Geologische Rundschau*, *67*(2), 531–546. https://doi.org/10.1007/BF01802803

Kennett, B. L. N., Engdahl, E. R., & Buland, R. (1995). Constraints on seismic velocities in the Earth from traveltimes. *Geophysical Journal International*, *122*(1), 108–124. https://doi.org/10.1111/j.1365-246X.1995.tb03540.x

Keranen, K. M., Klemperer, S. L., Julia, J., Lawrence, J. F., & Nyblade, A. A. (2009). Low lower crustal velocity across Ethiopia: Is the Main Ethiopian Rift a narrow rift in a hot craton? *Geochemistry, Geophysics, Geosystems*, *10*(5).

https://doi.org/10.1029/2008GC002293
Kieffer, B., Arndt, N. T., Lapierre, H., Bastien, F., Bosch, D., Pecher, A., … Meugniot, C. (2004). Flood and Shield Basalts from Ethiopia: Magmas from the African Superswell. *Journal of Petrology*, *45*(4), 793–834. https://doi.org/10.1093/petrology/egg112
Kim, S., Nyblade, A. A., Rhie, J., Baag, C.-E., & Kang, T.-S. (2012). Crustal S -wave velocity structure of the Main Ethiopian Rift from ambient noise tomography. *Geophysical Journal International*, *191*(2), 865–878. https://doi.org/10.1111/j.1365-246X.2012.05664.x
Korostelev, F., Weemstra, C., Leroy, S., Boschi, L., Keir, D., Ren, Y., … Ayele, A. (2015). Magmatism on rift flanks: Insights from ambient noise phase velocity in Afar region. *Geophysical Research Letters*, *42*(7), 2179–2188. https://doi.org/10.1002/2015GL063259
Landisman, M., Dziewonski, A., & Satô, Y. (1969). Recent Improvements in the Analysis of Surface Wave Observations. *Geophysical Journal of the Royal Astronomical Society*, *17*, 369–403. https://doi.org/10.4294/jpe1952.16.Special_1
Lavayssière, A., Rychert, C. A., Harmon, N., Keir, D., Hammond, J. O. S., Kendall, J.-M., … Leroy, S. (2018). Imaging lithospheric discontinuities beneath the northern East African Rift using S-to-P receiver functions. *Geochemistry, Geophysics, Geosystems*.
Lekic, V., French, S. W., & Fischer, K. M. (2011). Lithospheric Thinning Beneath Rifted Regions of Southern California. *Science*, *334*(November), 783–788. https://doi.org/10.7551/mitpress/8876.003.0036
Ligi, M., Bonatti, E., Bortoluzzi, G., Cipriani, A., Cocchi, L., Caratori Tontini, F., … Schettino, A. (2012). Birth of an ocean in the Red Sea: Initial pangs. *Geochemistry, Geophysics, Geosystems*, *13*(8), 1–29. https://doi.org/10.1029/2012GC004155
Mackenzie, G. D., Thybo, H., & Maguire, P. K. H. (2005). Crustal velocity structure across

the Main Ethiopian Rift: Results from two-dimensional wide-angle seismic modelling. *Geophysical Journal International*, *162*(3), 994–1006. https://doi.org/10.1111/j.1365-246X.2005.02710.x

Maguire, P. K. H., Keller, G. R., Klemperer, S. L., Mackenzie, G. D., Keranen, K. M., Harder, S., … Amha, M. (2006). Crustal structure of the northern Main Ethiopian Rift from the EAGLE controlled-source survey; a snapshot of incipient lithospheric break-up. *Geological Society, London, Special Publications*, *259*(1), 269–291. https://doi.org/10.1144/GSL.SP.2006.259.01.21

Makris, J., & Ginzburg, A. (1987). The Afar Depression: transition between continental rifting and sea-floor spreading. *Tectonophysics*, *141*(1–3), 199–214. https://doi.org/10.1016/0040-1951(87)90186-7

McClusky, S., Reilinger, R., Ogubazghi, G., Amleson, A., Healeb, B., Vernant, P., … Kogan, L. (2010). Kinematics of the southern Red Sea – Afar Triple Junction and implications for plate dynamics. *Geophysical Research Letters*, *37*, 1–5. https://doi.org/10.1029/2009GL041127

Mège, D., & Korme, T. (2004). Dyke swarm emplacement in the Ethiopian Large Igneous Province: Not only a matter of stress. *Journal of Volcanology and Geothermal Research*, *132*(4), 283–310. https://doi.org/10.1016/S0377-0273(03)00318-4

Meshesha, D., & Shinjo, R. (2007). Crustal contamination and diversity of magma sources in the northwestern Ethiopian volcanic province. *Journal of Mineralogical and Petrological Sciences*, *102*(5), 272–290. https://doi.org/10.2465/jmps.061129

Nishida, K. (2011). Two-dimensional sensitivity kernels for cross-correlation functions of background surface waves. *Comptes Rendus - Geoscience*, *343*(8–9), 584–590. https://doi.org/10.1016/j.crte.2011.02.004

Ogden, C. S., Bastow, I. D., Gilligan, A., & Rondenay, S. (2019). A Reappraisal of the H-κ

Stacking Technique: Implications for Global Crustal Structure. *Geophysical Journal International*, *219*, 1491–1513. https://doi.org/10.1093/gji/ggz364

Petersen, K. D., Armitage, J. J., Nielsen, S. B., & Thybo, H. (2015). Mantle temperature as a control on the time scale of thermal evolution of extensional basins. *Earth and Planetary Science Letters*, *409*, 61–70. https://doi.org/10.1016/j.epsl.2014.10.043

Pik, R., Deniel, C., Coulon, C., Yirgu, G., Hofmann, C., & Ayalew, D. (1998). The northwestern Ethiopian Plateau flood basalts: classification and spatial distribution of magma types. *Journal of Volcanology and Geothermal Research*, *81*(1–2), 91–111. https://doi.org/10.1016/S0377-0273(97)00073-5

Press, W. H., Teukolsky, S. A., Vetterling, W. T., & Flannery, B. P. (1992). Press. In *Numerical recipes in C: The art of scientific computing* (Second edn, pp. 444–455). Cambridge University Press.

Rooney, T. O. (2017). The Cenozoic magmatism of East-Africa: Part I — Flood basalts and pulsed magmatism. *Lithos*, *286–287*, 264–301. https://doi.org/10.1016/j.lithos.2017.05.014

Rooney, T. O. (2019). The Cenozoic Magmatism of East Africa: Part V – Magma sources and Processes in the East African Rift. *Lithos*. https://doi.org/10.1016/j.ctim.2019.102211

Rooney, T. O. (2020). The Cenozoic magmatism of East Africa: Part IV – The terminal stages of rifting preserved in the Northern East African Rift System. *Lithos*, *360–361*, 105381. https://doi.org/10.1016/j.lithos.2020.105381

Rooney, T. O., Bastow, I. D., Keir, D., Mazzarini, F., Movsesian, E., Grosfils, E. B., … Yirgu, G. (2014). The protracted development of focused magmatic intrusion during continental rifting. *Tectonics*, *33*, 875–897. https://doi.org/10.1002/2013TC003514.Received

Rooney, T. O., Furman, T., Yirgu, G., & Ayalew, D. (2005). Structure of the Ethiopian lithosphere: Xenolith evidence in the Main Ethiopian Rift. *Geochimica et Cosmochimica Acta*, *69*(15), 3889–3910. https://doi.org/10.1016/j.gca.2005.03.043

Rooney, T. O., Hanan, B. B., Graham, D. W., Furman, T., Blichert-toft, J., & Schilling, J. G. (2012). Upper mantle pollution during Afar plume-continental rift interaction. *Journal of Petrology*, *53*(2), 365–389. https://doi.org/10.1093/petrology/egr065

Rooney, T. O., Herzberg, C., & Bastow, I. D. (2012). Elevated mantle temperature beneath East Africa. *Geology*, *40*(1), 27–30. https://doi.org/10.1130/G32382.1

Rychert, C. A., Fischer, K. M., & Rondenay, S. (2005). A sharp lithosphere – asthenosphere boundary imaged beneath eastern North America. *Nature*, *436*, 542–545. https://doi.org/10.1038/nature03904

Rychert, C. A., Hammond, J. O. S., Harmon, N., Kendall, J.-M., Keir, D., Ebinger, C. J., … Stuart, G. W. (2012). Volcanism in the Afar Rift sustained by decompression melting with minimal plume influence. *Nature Geoscience*, *5*(6), 406–409. https://doi.org/10.1038/ngeo1455

Rychert, C. A., Harmon, N., Constable, Steve, & Wang, S. (2020). The nature of the Lithosphere-Asthenosphere Boundary. *Journal of Geophysical Research: Solid Earth*, 1–39. https://doi.org/10.1029/2018jb016463

Saito, M. (1988). DISPER80: a subroutine package for the calculation of seismic normal-mode solutions. In D. J. Doornbos (Ed.), *Seismological Algorithms: Computational Methods and Computer Programs* (pp. 293–319). Academic Press.

Samrock, F., Grayver, A. V., Eysteinsson, H., & Saar, M. O. (2018). Magnetotelluric Image of Transcrustal Magmatic System Beneath the Tulu Moye Geothermal Prospect in the Ethiopian Rift. *Geophysical Research Letters*, *45*(23), 12,847-12,855. https://doi.org/10.1029/2018GL080333

Samrock, F., Kuvshinov, A., Bakker, J., Jackson, A., & Fisseha, S. (2015). 3-D analysis and interpretation of magnetotelluric data from the Aluto-Langano geothermal field, Ethiopia. *Geophysical Journal International*, *202*(3), 1923–1948. https://doi.org/10.1093/gji/ggv270

Saria, E., Calais, E., Stamps, D. S., Delvaux, D., & Hartnady, C. (2014). Present-day kinematics of the East African Rift. *Journal of Geophysical Research : Solid Earth*, 1–17. https://doi.org/10.1002/2013JB010901.Received

Siegburg, M., Gernon, T. M., Bull, J. M., Keir, D., Barfod, D. N., Taylor, R. N., … Ayele, A. (2018). Geological evolution of the Boset-Bericha Volcanic Complex, Main Ethiopian Rift:40Ar/39Ar evidence for episodic Pleistocene to Holocene volcanism. *Journal of Volcanology and Geothermal Research*, *351*, 115–133. https://doi.org/10.1016/j.jvolgeores.2017.12.014

Sim, S. J., Spiegelman, M., Stegman, D. R., & Wilson, C. (2020). The influence of spreading rate and permeability on melt focusing beneath mid-ocean ridges. *Physics of the Earth and Planetary Interiors*, *304*. https://doi.org/10.1016/j.pepi.2020.106486

Sparks, D. W., & Parmentier, E. M. (1991). Melt extraction from the mantle beneath spreading centers. *Earth and Planetary Science Letters*, *105*(4), 368–377. https://doi.org/10.1016/0012-821X(91)90178-K

Stuart, G. W., Bastow, I. D., & Ebinger, C. J. (2006). Crustal structure of the northern Main Ethiopian Rift from receiver function studies. *Geological Society, London, Special Publications*, *24*(4), 623–626.

Tarantola, A., & Valette, B. (1982). Generalized nonlinear inverse problems solved using the least squares criterion. *Reviews of Geophysics*, *20*(2), 219–232. https://doi.org/10.1029/RG020i002p00219

Tesfaye, S., Harding, D. J., & Kusky, T. M. (2003). Early continental breakup boundary and migration of the Afar triple junction, Ethiopia. *Bulletin of the Geological Society of America*, *115*(9), 1053–1067. https://doi.org/10.1130/B25149.1

Tromp, J., Luo, Y., Hanasoge, S. M., & Peter, D. (2010). Noise cross-correlation sensitivity kernels. *Geophysical Journal International*, *183*(2), 791–819. https://doi.org/10.1111/j.1365-246X.2010.04721.x

Ukstins, I. A., Renne, P. R., Wolfenden, E., Baker, J., Ayalew, D., & Menzies, M. (2002). Matching conjugate volcanic rifted margins: 40Ar/39Ar chrono-stratigraphy of pre- and syn-rift bimodal flood volcanism in Ethiopia and Yemen. *Earth and Planetary Science Letters*, *198*(3–4), 289–306. https://doi.org/10.1016/S0012-821X(02)00525-3

Varga, R. J., Horst, A. J., Gee, J. S., & Karson, J. A. (2008). Direct evidence from anisotropy of magnetic susceptibility for lateral melt migration at superfast spreading centers. *Geochemistry, Geophysics, Geosystems*, *9*(8), 1–8. https://doi.org/10.1029/2008GC002075

Vigny, C., Huchon, P., Ruegg, J., Khanbari, K., & Asfaw, L. (2006). Confirmation of Arabia plate slow motion by new GPS data in Yemen. *Journal of Geophysical Research*, *111*(April 2005), 1–14. https://doi.org/10.1029/2004JB003229

Wang, S., Constable, Steven, Rychert, C. A., & Harmon, N. (2020). A Lithosphere-Asthenosphere Boundary and Partial Melt Estimated Using Marine Magnetotelluric Data at the Central Middle Atlantic Ridge. *Geochemistry, Geophysics, Geosystems*, *21*(9), 1–7. https://doi.org/10.1029/2020GC009177

Wang, T., Gao, S. S., Yang, Q., & Liu, K. H. (2021). Crustal structure beneath the Ethiopian Plateau and adjacent areas from receiver functions: Implications for partial melting and magmatic underplating. *Tectonophysics*. https://doi.org/10.1016/j.tecto.2021.228857

Wang, Y., Forsyth, D. W., & Savage, B. (2009). Convective upwelling in the mantle beneath the Gulf of California. *Nature*, *462*(7272), 499–501. https://doi.org/10.1038/nature08552

Wessel, P., & Smith, W. H. F. (2013). Generic Mapping Tools : Improved Version Released, *94*(45).

Whaler, K. A., & Hautot, S. (2006). The electrical resistivity structure of the crust beneath the northern Main Ethiopian Rift. *Geological Society, London, Special Publications*, *259*, 293–305.

Wolfenden, E., Ebinger, C. J., Yirgu, G., Deino, A., & Ayalew, D. (2004). Evolution of the northern Main Ethiopian rift: birth of a triple junction. *Earth and Planetary Science Letters*, *224*(1–2), 213–228. https://doi.org/10.1016/j.epsl.2004.04.022

Wolfenden, E., Ebinger, C. J., Yirgu, G., Renne, P. R., & Kelley, S. P. (2005). Evolution of a volcanic rifted margin: Southern Red Sea, Ethiopia. *Bulletin of the Geological Society of America*, *117*(7–8), 846–864. https://doi.org/10.1130/B25516.1

Yang, Y., & Forsyth, D. W. (2006). Regional tomographic inversion of the amplitude and phase of Rayleigh waves with 2-D sensitivity kernels. *Geophysical Journal International*, *166*(3), 1148–1160. https://doi.org/10.1109/TIM.2006.876410

Yoshizawa, K., & Kennett, B. L. N. (2002). Determination of the influence zone for surface wave paths. *Geophysical Journal International*, *149*(2), 440–453. https://doi.org/10.1046/j.1365-246X.2002.01659.x

Zhou, Y., Dahlen, F. A., & Nolet, G. (2004). Three-dimensional sensitivity kernels for surface wave observables. *Geophysical Journal International*, *158*(1), 142–168. https://doi.org/10.1111/j.1365-246X.2004.02324.x

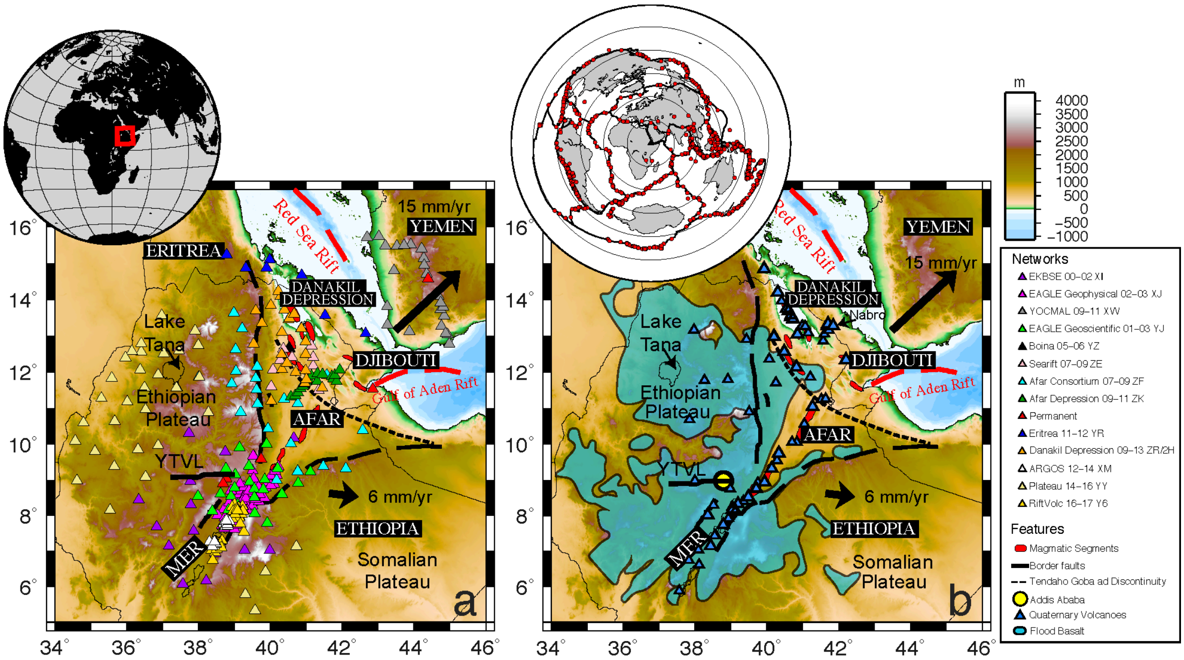


*Figure 1a) Seismic station map of the northern East African Rift. Thick black lines show border faults, red polygons crustal magmatic segments, and dashed lines the Tendaho-Goba'ad discontinuity (TGD). Stations are triangles coloured to their project deployment with the final 4 networks (Danakil depression–RiftVolc) new networks not used for ambient noise or teleseismic tomography. Arrows indicate extension rates relative to the stationary Nubian plate* (Jestin et al., 1994; Saria et al., 2014; Vigny et al., 2006). *(b) Geological map. Volcanoes are represented by blue triangles and crustal magmatic segments red polygons. Flood basalt provinces are shown in blue. Addis Ababa is marked by yellow circle. Inset figure red dots show locations of the 1053 earthquakes used in this study. Arrows again indicate extension rates relative to the stationary Nubian plate* (Jestin et al., 1994; Saria et al., 2014; Vigny et al., 2006).

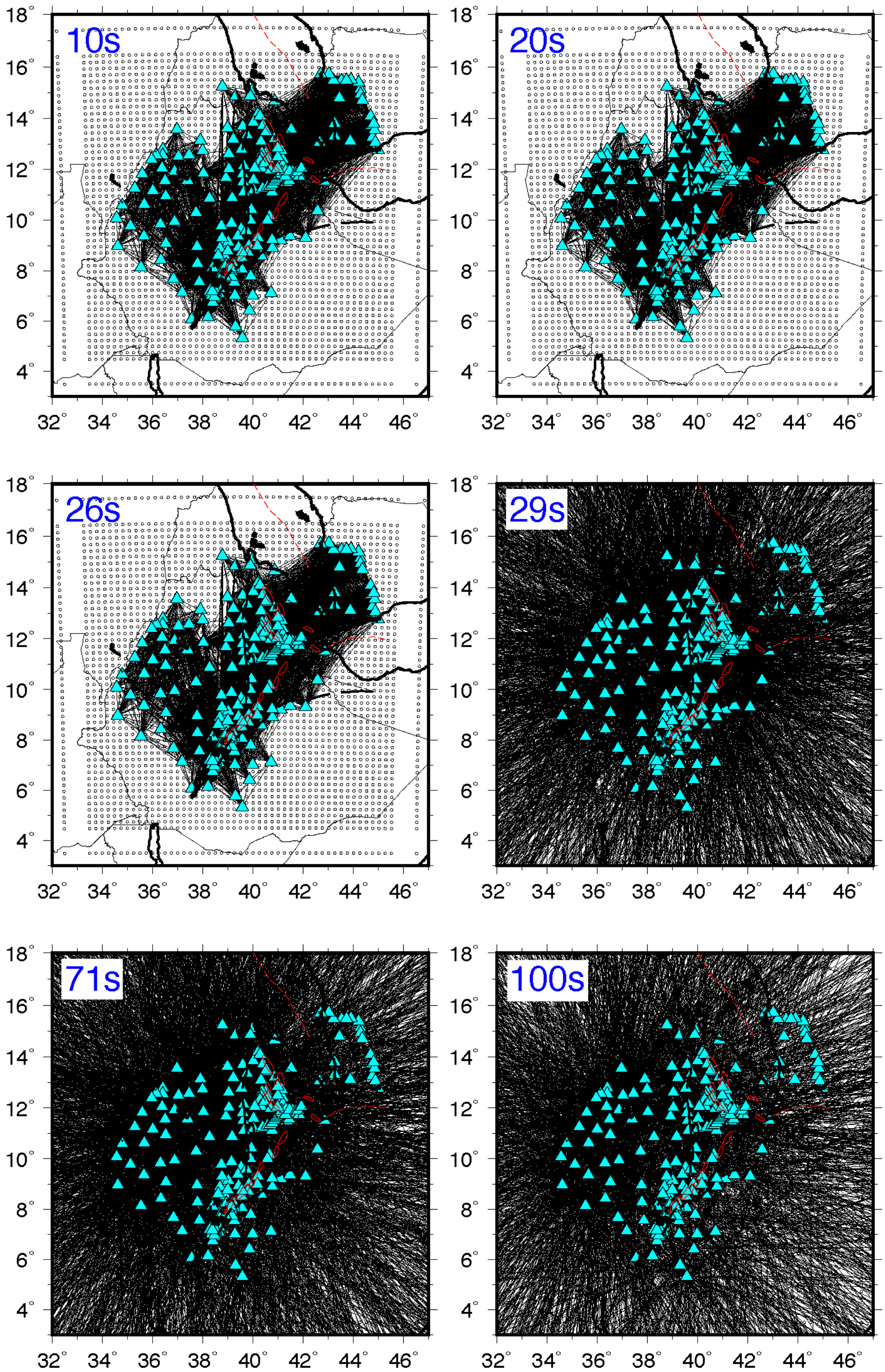


*Figure 2 Nodal grid at 0.25 ° spacing with ray paths for ambient noise (a–c, 8, 20 and 26s) and teleseisms (d–f, 29, 71 and 100 s) overlain as black lines. Blue triangles indicate stations and red polygons the crustal magmatic segments.*

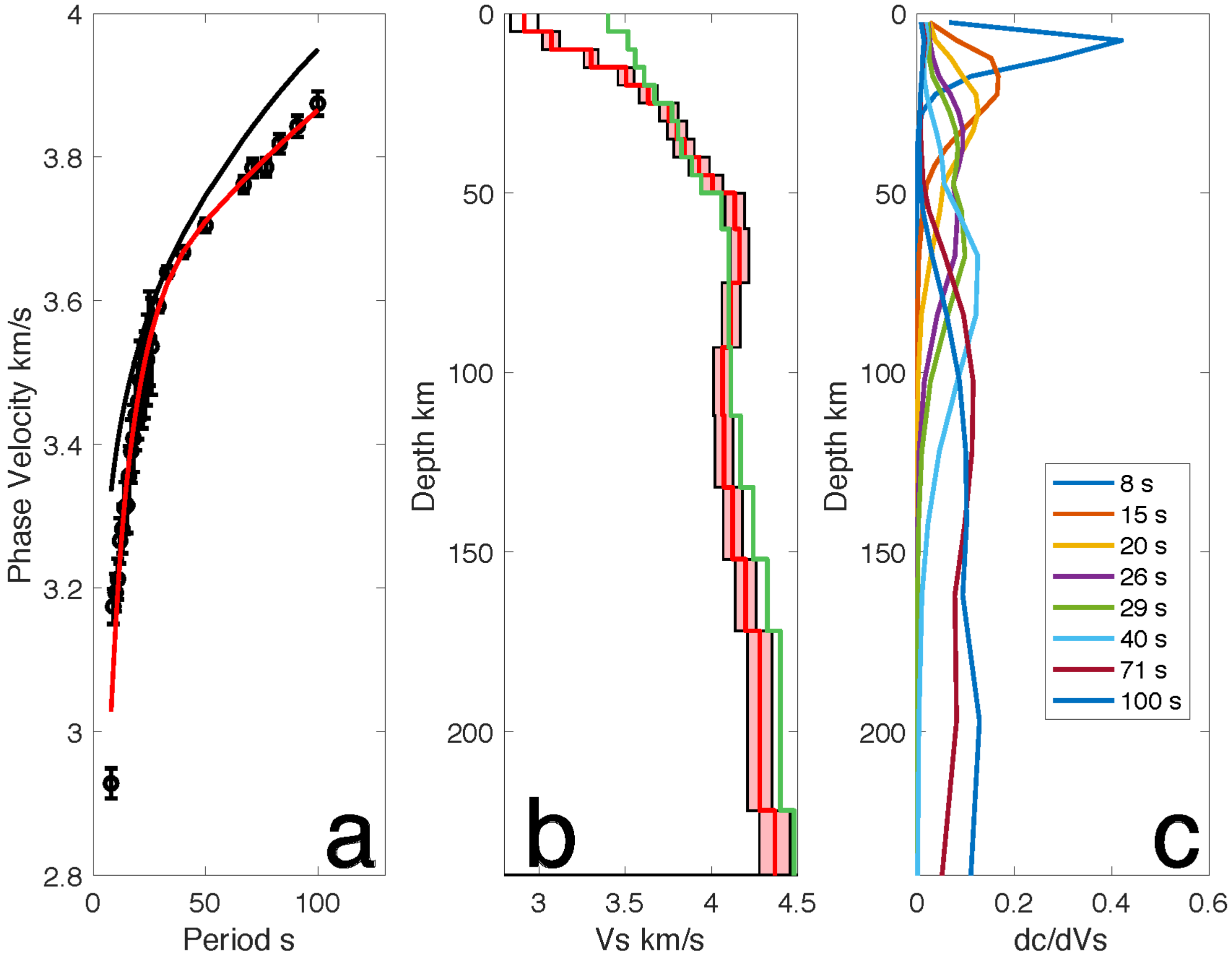


*Figure 3a) Average 1-D phase velocity for the study area with 3σ error bars (circles), starting model (black line) with our best fit shear velocity model dispersion overlain (red line). (b) Best fit shear velocity model for the study area (red line) and formal 2σ error bounds (thin black lines and shaded area). Green line is initial starting model using the average shear velocity from Chambers et al., (2019) and Gallacher et al., (2016). (c) Sensitivity kernels for Rayleigh waves at selected periods.*

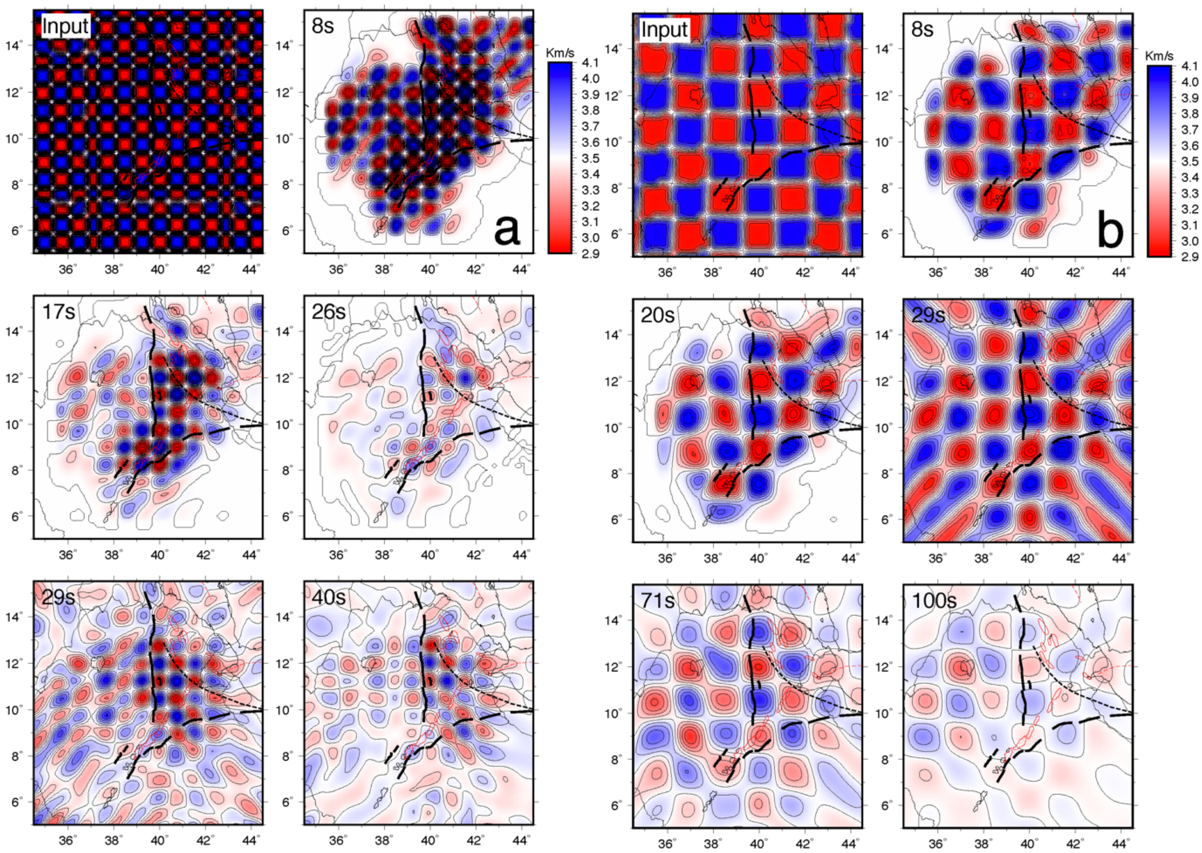


*Figure 4 a) Checkerboard tests at 70 km × 70 km for phase velocities from ambient noise (8–26s) and teleseisms (29 and 40 s) which are sensitive to crustal and upper most mantle depths (left 2 panels). Within the rift and eastern part of the Ethiopian Plateau we can resolve the checkerboards with confidence. Outside these areas features should not be interpreted. Right 2 panels: b) Checkerboard tests at 165 km × 165 km (~1.5° x 1.5°) for phase velocities from ambient noise (8–20 s) and Teleseisms (29-100 s) for the minimum and maximum periods. Within the rift and eastern part of the Ethiopian Plateau we can resolve the checkerboards with confidence to 100 s period, although the magnitude of the anomaly weakens with increasing period. Thick black lines show border faults, red polygons crustal magmatic segments, and dashed lines the Tendaho-Goba'ad discontinuity (TGD). For further checker board tests at 110 km and 220 km spacings see supplementary Figures S4 and S5.*

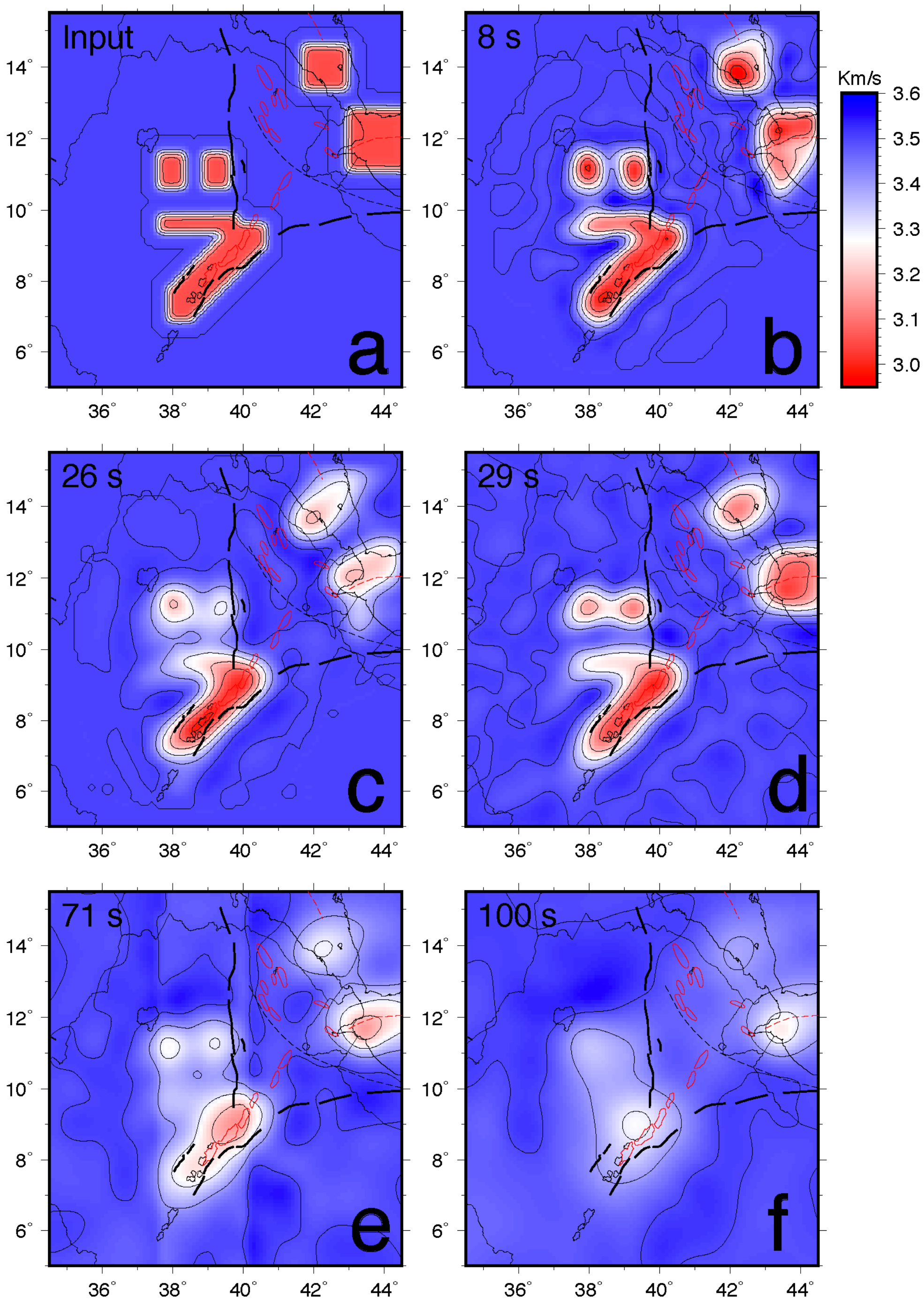


*Figure 5 Synthetic recovery tests inputting slow velocity anomalies beneath the Main Ethiopian Rift, YTVL, Red Sea Rift, Gulf of Aden Rift and beneath the eastern part of the Ethiopian Plateau at 8, 26, 29, 71 and 100 s period. Thick black lines show border faults, red polygons crustal magmatic segments, and dashed lines the Tendaho-Goba'ad discontinuity (TGD). Off rift features are resolvable at short periods equivalent to crustal depths though smear together at longer periods. The MER and Gulf of Aden anomalies are visible at all periods with decreasing amplitude at longer periods.*

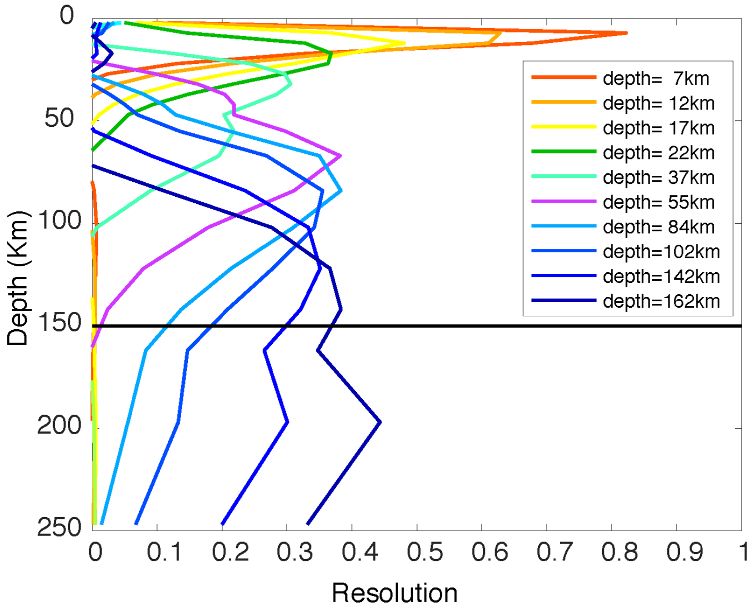


*Figure 6 Spike test for depths of 7, 12, 17, 22, 37, 55, 84, 102, 142 and 162 km depth. Vertical resolution ranges from ±10 km at the shallowest depths (7-22 km) and ±50 km for the deepest slices at 142-162 km depth.*

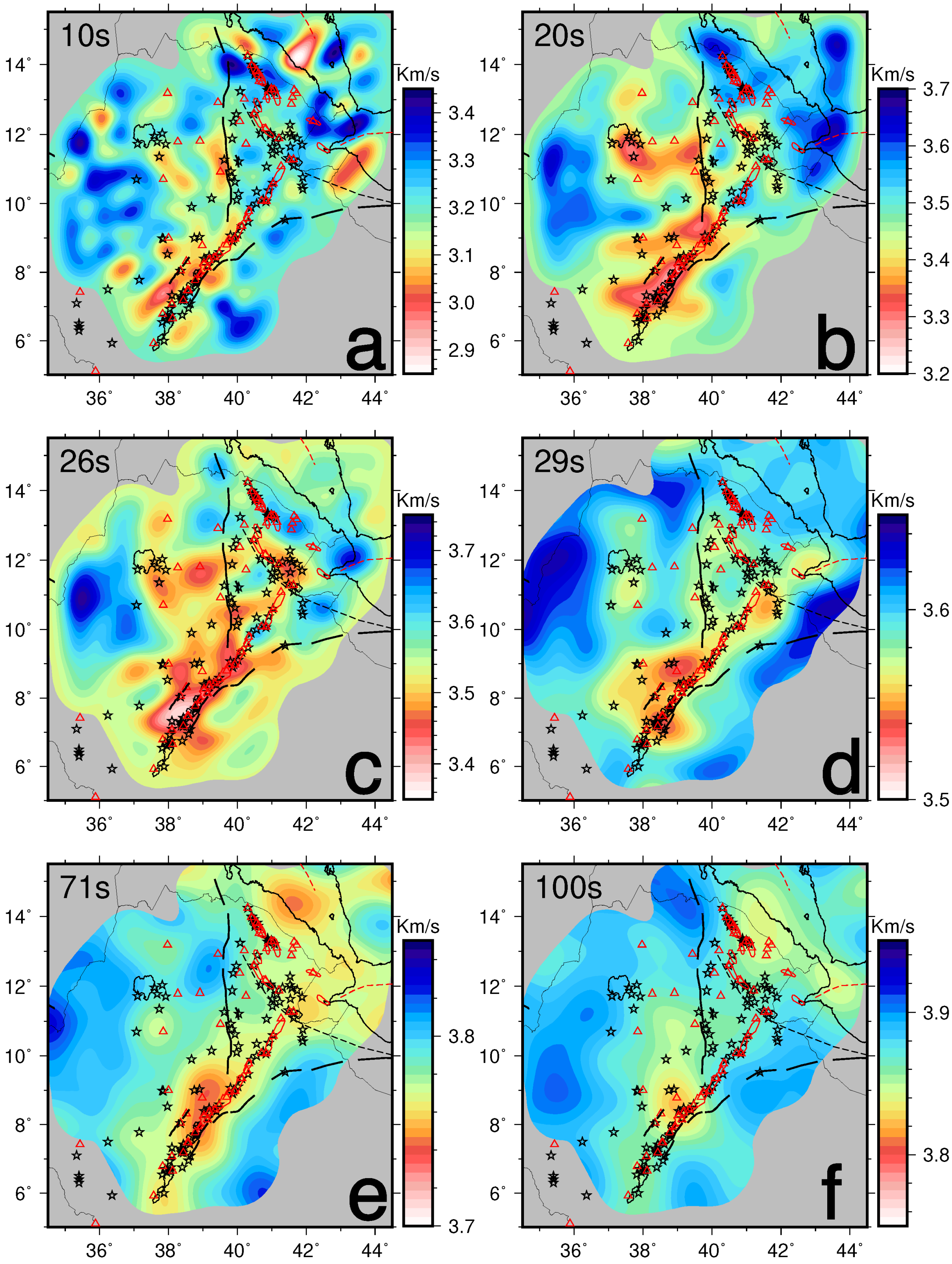


*Figure 7 Phase velocity maps generated by tomographically inverting dispersion curves from ambient noise (10, 20, 26s) and teleseisms (29, 71 and 100 s). Models have been cropped to the 2σ standard error contour. Pink and red colours are slower*

*velocities and blue faster velocities. Thick black lines indicate border faults, red polygons crustal magmatic segments, dashed lines the Tendaho-Goba'ad discontinuity (TGD), red triangles volcanoes, and black stars geothermal activity.*

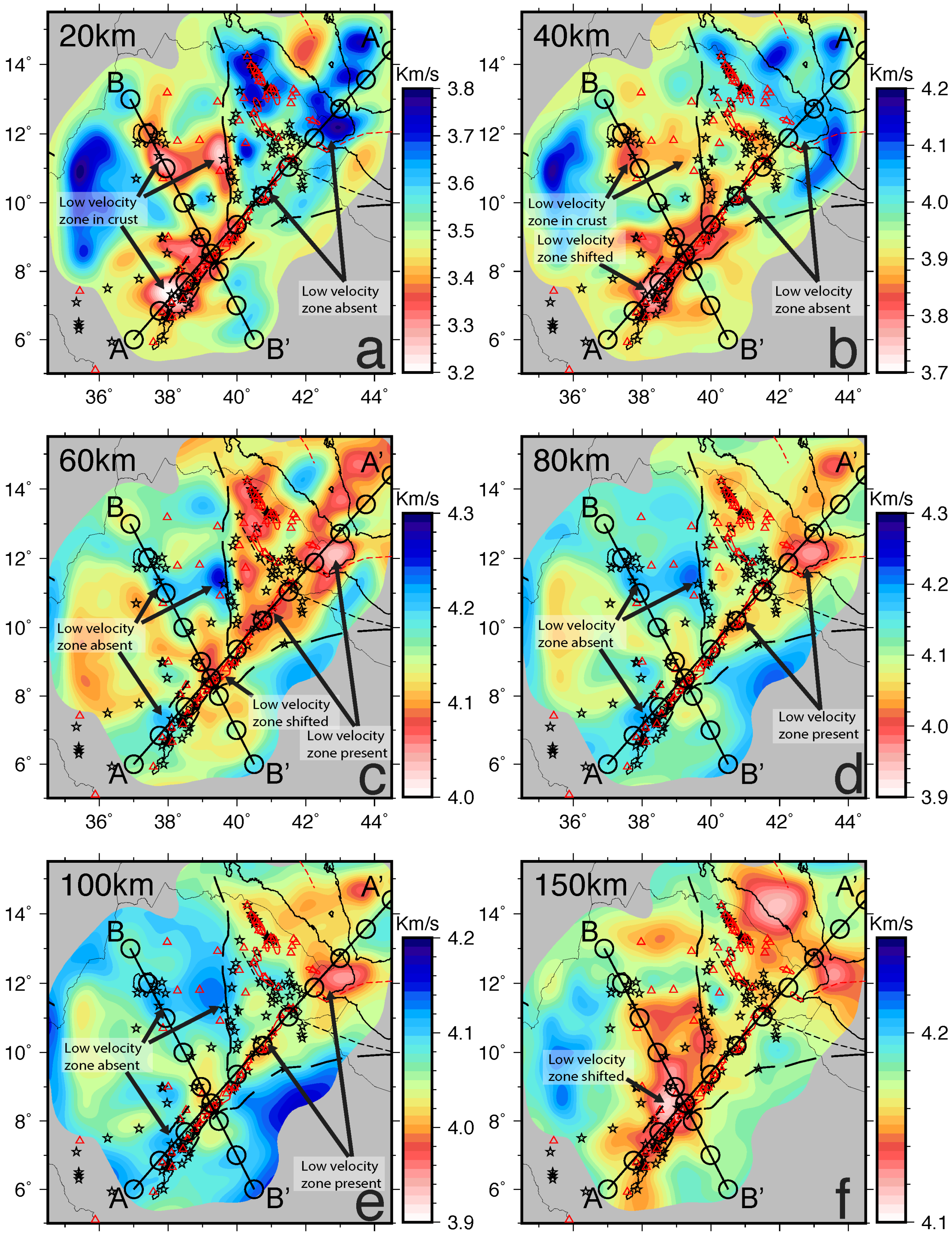

*Figure 8 Interpolated absolute shear wave velocity at 20, 40, 60, 80, 100 and 150 km. Models have been cropped to the standard error contour. Pink and red colours indicates slower velocities and blue faster velocities. Thick black lines indicate border faults. 2 profiles (thin black lines with black rings) are the cross-section locations for Figure 9. Red polygons indicate crustal magmatic segments, red triangles volcanoes, and black stars geothermal activity. Arrows indicate areas discussed in the text. See supplementary Figure S6 for slices at 10 km depth intervals.*

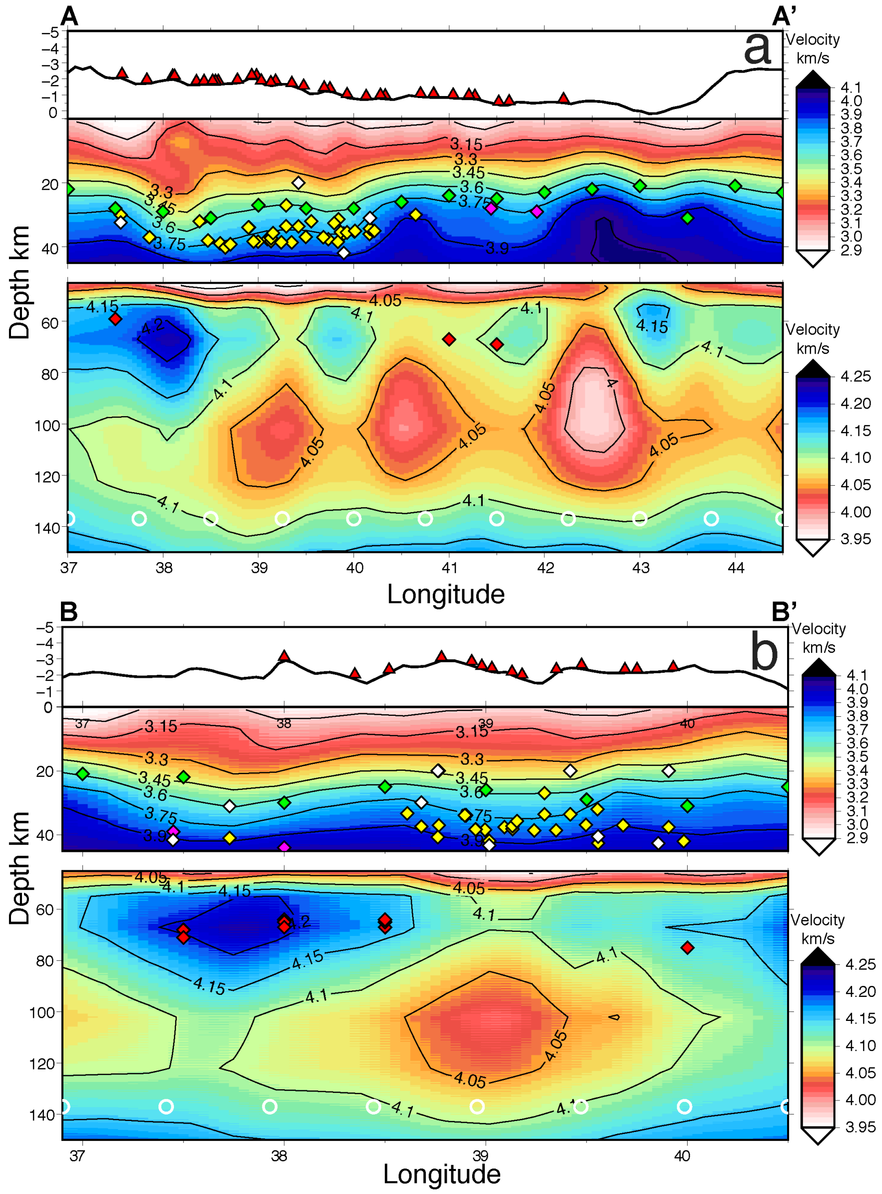


*Figure 9 Cross-sections through the interpolated absolute shear velocity depth slices a) along the rift and b) across the rift (See Figure 8* for *locations). The cross-sections have been split into crustal section (0-45 km depth, top panel) and mantle (45–150 km depth, bottom panel) for display purposes. Red and pink colours indicate slower velocities, and blue faster velocities. Red triangles above section indicate quaternary volcanoes with topography as black line. Thin lines are velocity contours and diamonds represent previous receiver function results for the Moho in top sections (green* (Lavayssière et al.,

2018)*, magenta* (Hammond, et al., 2011)*, yellow* (Stuart et al., 2006)*, white* (Ogden et al., 2019)*) and LAB in bottom sections (red* (Lavayssière et al., 2018)*). White rings are the same as black rings in Figure 8, for location reference.*